EES Batteries

REVIEW

View Article Online
View Journal

Cite this: DOI: 10.1039/d6eb00030d

Electrolyte-centric strategies for high-energy-density lithium metal batteries

Qidong Ruan,†[a,b] Yong Wu, †[c] Yifan Wang,[a,b] Hao Cheng *[a,b] and Yingying Lu *[a,b]

Achieving lithium metal batteries (LMBs) with energy densities beyond 500 Wh kg^{-1} requires electrolyte systems capable of operating under increasingly stringent conditions, including thin lithium metal anodes, lean electrolyte configurations, and high-voltage layered-oxide cathodes. In this context, electrolyte design has evolved from incremental component optimization to a system-level, electrolyte-centric strategy that couples bulk chemistry, interfacial processes, and manufacturability considerations. This review provides a comprehensive and critical overview of recent advances in electrolyte design for high-energy-density LMBs, organized across three major pathways: liquid electrolytes, polymer and quasi-solid electrolytes, and inorganic solid-state electrolytes. For liquid systems, progress in solvation-structure engineering, ionic-cluster regulation, and interfacial chemistry has enabled improved stability under high voltage and low electrolyte loading. Polymer-based systems offer enhanced safety and interfacial compatibility, though challenges remain in achieving sufficient room-temperature ionic conductivity. Inorganic solid electrolytes deliver superior thermal and electrochemical stability, yet are constrained by interfacial resistance, mechanical coupling, and air stability. Beyond individual material classes, we identify six cross-cutting challenges governing practical LMB deployment, including interfacial instability, integrated solvation-network engineering, performance–safety–cost synergy, data-driven discovery, scalable manufacturing compatibility, and solid–solid interface limitations. By consolidating mechanistic insights and system-level design principles, this review aims to provide a coherent framework to guide the development of next-generation, high-energy, and practically viable lithium metal batteries.

Received 5th February 2026,
Accepted 24th March 2026

DOI: 10.1039/d6eb00030d

rsc.li/EESBatteries

Broader context

The global transition to sustainable energy and electrified transportation is fundamentally constrained by the performance of current energy storage systems. As conventional lithium-ion batteries approach their intrinsic material limits, breaking the critical 500 Wh kg^{-1} barrier is essential for extending vehicle range and enabling advanced aerospace applications. Lithium metal batteries, leveraging the anode's ultra-high capacity, offer the most viable pathway. However, this pursuit transcends simple component replacement. It demands a paradigm shift towards a holistic, electrolyte-centric design philosophy. The electrolyte is no longer a passive component but the central enabler, requiring co-optimization of bulk ion transport, robust interfacial stabilization at both electrodes, and compatibility with scalable manufacturing processes. Ultimately, pioneering advances in electrolyte science are pivotal to unlocking the next generation of batteries: devices that are simultaneously safer, more powerful, durable, and commercially viable, thereby accelerating progress toward a fully decarbonized future.

1. Introduction

Driven by the rapid expansion of electric transportation, renewable-energy storage, and advanced aerospace technologies, next-generation energy-storage systems urgently require rechargeable batteries with substantially higher specific energy.[1] Conventional lithium-ion batteries (LIBs) are approaching their practical limits, creating barriers to meeting ever-increasing demands for both energy density and safety.[2,3] Lithium metal batteries (LMBs) capable of ≥500 Wh kg^{-1} are widely regarded as a compelling pathway to surpass the

[a]State Key Laboratory of Chemical Engineering, Institute of Pharmaceutical Engineering, College of Chemical and Biological Engineering, Zhejiang University, 310027 Hangzhou, Zhejiang, China. E-mail: yingyinglu@zju.edu.cn
[b]Zhejiang Key Laboratory of Intelligent Manufacturing for Functional Chemicals, ZJU-Hangzhou Global Scientific and Technological Innovation Center, Zhejiang University, Hangzhou, 311215 China. E-mail: bob_hao@zju.edu.cn
[c]Suzhou Laboratory, Suzhou 215000, China
†These authors contributed equally to this work.

current energy-density ceiling, owing to the ultralow redox potential of lithium (−3.04 V *vs.* SHE) and its exceptionally high theoretical specific capacity (~3860 mAh g^{-1}), which together provide the material's foundation for system-level energy-density escalation.[4–6] For the mainstream "intercalation-oxide cathode (*e.g.*, $LiCoO_2$ or Ni-rich layered oxides such as $LiNi_{0.8}Co_{0.1}Mn_{0.1}O_2$, NCM811) paired with a Li-metal anode" configuration, the determinants of system energy density are not single-material parameters but the coupled optimization of materials, interfaces, and operating constraints. Under thin-Li, lean electrolyte (E/C), and high cut-off-voltage conditions, the electrolyte must simultaneously sustain high Li^+ flux, enable controlled solvation/desolvation kinetics, and stabilize both the solid–electrolyte interphase (SEI) and the cathode–electrolyte interphase (CEI). Therefore, the electrolyte challenge in practical high-energy LMBs is intrinsically dual-sided: it must not only suppress dendrite formation and parasitic reduction at the Li-metal anode, but also resist oxidative decomposition and maintain CEI integrity at high-voltage cathodes. In commercial-type electrolytes, a high cut-off voltage often triggers severe oxidative decomposition at the electrolyte/cathode interface, aggravated by the high catalytic activity of transition-metal surfaces, whereas, on the Li anode side, uncontrolled dendrite growth and parasitic reactions result in low coulombic efficiency and poor cycle life.[7–9]

Consequently, electrolyte instability stands out as a principal obstacle to high-energy LMBs; indeed, the integrated performance of the electrolyte is a core limiting factor for achieving reversible ≥500 Wh kg^{-1} systems.[10] The electrolyte not only dictates Li-ion transport behavior, but also exerts a profound influence on interfacial stability, thermal safety, and overall cycling durability. Electrolyte modification *via* functional additives is widely regarded as one of the most effective approaches for addressing the foregoing challenges, and a variety of additives have already delivered demonstrable gains in electrochemical performance.[11–14] In parallel, high-concentration electrolytes (HCEs) and solid electrolytes have shown considerable potential for suppressing dendrite formation at the Li anode and mitigating electrolyte decomposition.[15–17] Solid-state electrolytes (SSEs)—including polymer-based SSEs (PSSEs) and inorganic SSEs (ISSEs)—offer intrinsic advantages in safety and high-voltage tolerance, thereby alleviating the safety risks inherent to conventional liquid electrolytes.[18,19] PSSEs provide compliant matrices and Lewis acid/base sites that promote wetting and selective interphase formation, yielding excellent interfacial compatibility; however, their room-temperature ionic conductivity typically requires further enhancement.[20] ISSEs leverage robust thermal/electrochemical stability to improve safety and widen the electrochemical stability window, yet high interfacial resistance at room temperature, manufacturability constraints, and environmental sensitivity—most notably the air/moisture reactivity of sulfides—remain core bottlenecks to high specific energy and scalable deployment.[21] Moreover, even in dense inorganic SSE bodies, fast grain-boundary pathways can facilitate filamentary Li penetration, posing dendrite and short-circuit risks.[22,23] These considerations underscore the need for an integrated electrolyte-design strategy that couples molecular-scale coordination control, nanoscale ionic-structure optimization, and targeted interfacial engineering to realize truly high-energy and intrinsically safe LMBs.

To avoid an overly broad scope, throughout this review "high-energy lithium batteries" specifically refer to Li-metal anodes paired with commercialized layered-oxide cathodes (represented by Ni-rich NCM/NCMA and LCO/LNO); chemistries such as Li–S, Li–O_2, and phosphate/spinel cathodes are outside our scope.

Against this backdrop, three complementary electrolyte pathways have emerged. (i) Liquid electrolytes use co-optimized solvents/salts/diluents and functional additives to engineer solvation (*e.g.*, enhanced anion participation and tuned ionic clustering) and to program SEI/CEI so as to reorder interfacial reactions, reconciling low-temperature kinetics with high-voltage stability. (ii) Polymer/gel (quasi-solid) electrolytes leverage tunable segment polarity and Lewis acid/base sites to improve wetting and selective interphase formation, and pursue a balance between room-temperature conductivity and mechanical robustness *via* polymer-solvation and ion-channel design. (iii) Inorganic solid-state electrolytes provide intrinsic safety and wide electrochemical windows, but face engineering challenges in room-temperature interfacial resistance, processing/environmental sensitivity, and grain-boundary/porosity-related failure.

Guided by an electrolyte-centric design philosophy, this review systematically maps progress for achieving reversible 500 Wh kg^{-1} LMBs. We first examine liquid-electrolyte strategies, emphasizing regulation of solvation structures, ionic-cluster engineering, and the development of novel lithium salts and functional additives. We then extend the discussion to quasi-solid and polymer electrolytes, focusing on intermolecular interactions and chain-segment solvation. The third section critically evaluates inorganic SSEs, covering ion-transport mechanisms, air/moisture stability, and interfacial modification (Fig. 1). Through this cross-cutting synthesis and integration, the review aims to provide system-level guidance and theoretical foundations for electrolyte architectures that deliver high energy, high stability, and practical operability in LMBs.

2. Liquid electrolyte design

Liquid electrolytes have been the mainstay of commercial lithium-ion batteries due to their high ionic conductivity, good electrode wettability, and tunable formulations. Liquid electrolytes continue to play an important role in bridging the gap between today's technologies and future performance targets as the quest for next-generation LMBs incorporating gravimetric energy densities above 500 Wh kg^{-1} continues. However, they also bear intrinsic safety concerns and possess poor compatibility with Li-metal anodes. Besides, there are severe challenges when paired with high-voltage/high-capacity

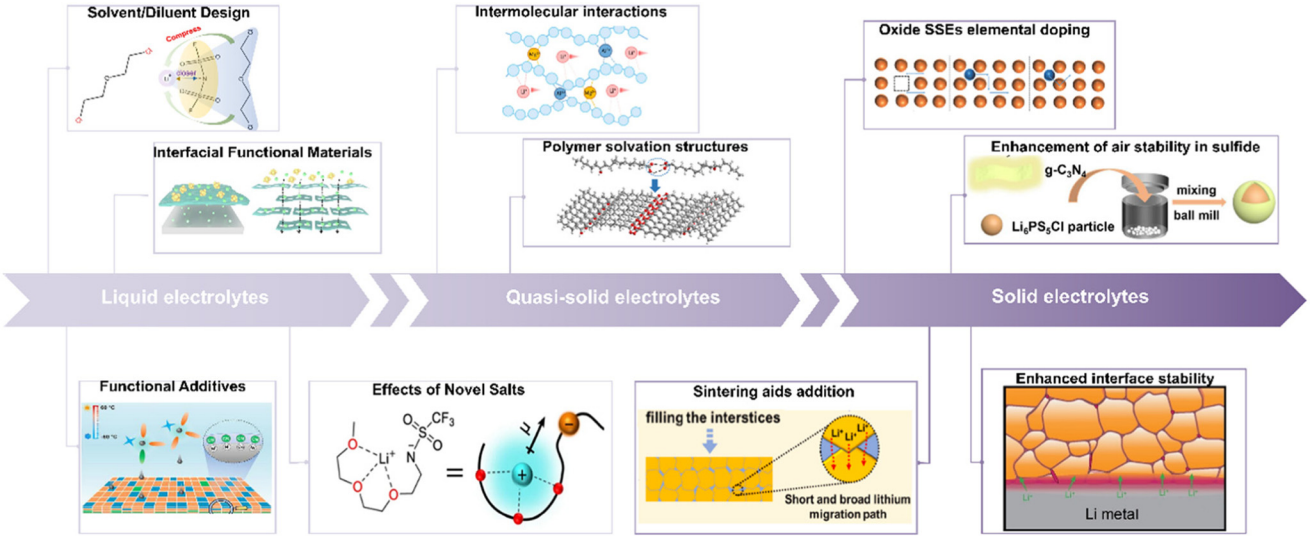

Fig. 1 Brief schematic diagram of the development of high-energy-density LMBs electrolytes. Data from ref. 24–33.

cathodes—evinced typically by rapid capacity fade and rate limitations deriving from interfacial kinetic and morphological instabilities.[34] Those two failure modes originate from the fundamental instability of Li^0 (metallic lithium) against the electrolyte: uncontrolled parasitic reactions that drive continuous growth of the SEI layer and sluggish ion transport.[35,36] Several advances in electrolyte chemistry have thus far allowed significant progress in stabilizing the Li–metal interface when using high-voltage cathodes and further increasing energy density and cycle life of LMBs: HCEs,[37–39] localized HCEs (LHCEs),[40–43] novel functional additives,[44,45] and artificial SEI or surface coating on lithium metal.[46] This part reviews the latest progress in liquid electrolyte design, focusing on the strategies of interfacial stability enhancement, dendrite growth suppression, and expansion of the electrochemical stability window toward supporting high-energy LMB systems. Special attention is also paid to the cathode-side oxidative stability challenge, because high-voltage layered-oxide compatibility is equally decisive for practical high-energy LMB operation.

Framed from an implementation ("how to land in practice") perspective, we organize the discussion into four levers: (i) solvent/salt/diluent design, (ii) functional additives, (iii) interfacial functional materials, and (iv) effects of novel salts and functional salt additives. These levers act from intrinsic-system tuning, chemical steering, orthogonal interfacial reconstruction, and salt-chemistry modulation, respectively, and coherently regulate the causal chain "primary solvation shell → mesoscale ionic clusters (contact ion pairs, CIP; aggregates, AGG; compact ion-pair aggregates, CIPA) → SEI/CEI layer → transport/kinetics", aiming to realize high energy density and long life under thin-Li, lean-electrolyte (low electrolyte/cathode, E/C), high-loading cathodes, high-voltage cutoffs, and wide-temperature operation. From a mechanistic standpoint, these four design levers should not be viewed as isolated formulation strategies, but as distinct entry points for regulating the same multiscale physicochemical pathway. Solvent/salt/diluent design primarily determines the primary solvation shell and the evolution of ion-association motifs and mesoscale clusters; functional additives mainly regulate the sequence of interfacial decomposition and the origin of SEI/CEI-forming species; interfacial functional materials more directly reshape local Li^+ flux, localized solvation environments, and interphase growth geometry at the electrode surface; and novel salts modify not only Li^+ coordination and ionic dissociation, but also the intrinsic electrochemical stability window and preferential decomposition chemistry. In this sense, the diverse liquid-electrolyte strategies discussed below are fundamentally connected through a shared objective: to program how solvation structure evolves into interphase chemistry and, ultimately, into transport kinetics and practical cell stability under thin-Li, lean-electrolyte, and high-voltage conditions.

2.1 Solvent/diluent design

Solvent and diluent engineering directly reshapes the local Li^+ coordination environment and the larger-scale ionic organization. Common objectives are to minimize "free" solvent, increase anion participation in the primary solvation shell, and induce a dense, inorganic-rich (LiF/Li_2O, *etc.*) SEI/CEI that lowers desolvation barriers, accelerates interfacial Li^+ transport, and suppresses electrolyte oxidation/corrosion at high voltage.

To avoid conceptual ambiguity, it is meaningful to distinguish three hierarchical levels of electrolyte organization in liquid LMB electrolytes. The primary solvation shell refers to the nearest-neighbour coordination environment of Li^+, namely, the identities and coordination numbers of solvent molecules and anions directly surrounding Li^+. CIP and AGG describe local ion-association motifs beyond the single-ion picture: CIP denotes direct Li^+–anion contact pairs, whereas

AGG represents higher-order ionic aggregates involving multiple Li^+/anion interactions. By contrast, CIPA refers to more compact and densely packed nanometre-scale aggregates, which extend beyond local coordination and reflect a mesoscopic packing state of ion pairs rather than merely a higher AGG fraction.

These hierarchical structures are distinguished by complementary characterization tools and influence interfacial behaviour at different, yet strongly coupled, scales. Raman spectroscopy is particularly useful for resolving free anions, CIPs and AGGs through characteristic peak shifts and deconvolution, while NMR provides coordination-sensitive information on the local chemical environment. MD simulations further quantify coordination numbers, radial distribution functions, Li^+–Li^+ distances and cluster-size statistics, and are especially important for identifying compact mesoscopic aggregates such as CIPA. In mechanistic terms, the primary solvation shell predominantly governs the first-step desolvation barrier and the identities of species that are preferentially reduced or oxidized to form SEI/CEI precursors. The CIP/AGG population more directly affects charge-carrier nature, Li^+ transport mode and the spatial uniformity of interfacial reactions. Mesoscopic compact aggregates such as CIPA can further enable collective interfacial reduction behaviour and rapid construction of thin, inorganic-rich interphases, thereby coupling cluster topology with both transport kinetics and SEI/CEI homogeneity. Although these levels are analytically distinguishable, they are intrinsically coupled in practice: local coordination chemistry governs cluster evolution, while cluster topology in turn feeds back into interphase formation and ion-transport behaviour.

Regarding weakly coordinating and end-group–engineered solvents, Yang *et al.* introduced a minimally coordinating co-solvent, chlorodiethoxyethane (ClDEE), to compress Li^+–FSI^- coordination and enrich anions within the Li^+ primary solvation shell (Fig. 2a). This "compressed solvation structure" reduces the solvent fraction in the inner sheath, suppressing solvent reduction at Li and promoting early, complete LiFSI decomposition to yield a uniform, LiF/Li_2O-rich inorganic SEI. A pouch cell delivered 510.3 Wh kg^{-1} and remained stable after 100 cycles.[24] Zhang *et al.* synthesized a trifluoromethyl end-capped ether (TMEE, 1,1,1-trifluoro-2-(2-methoxyethoxy) ethane) on a DME backbone to impose strong electron-withdrawing and "de-solvating" effects (Fig. 2b), shifting the coordination toward anion-dominated solvation and forming a bilayer SEI (Li_2O-rich outer, amorphous inner, Fig. 2c) while suppressing Al current-collector corrosion; with 50 μm Li and high-loading NMC811, >400 cycles at 1 C were achieved in 14 Ah pouches with >510 Wh kg^{-1}.[34] Wu *et al.* used terminal-group substitution to tailor solvation, designing weakly coordinating, non-flammable fluorosulfonyl (FSO_2^-) solvents. Amine-substituted variants—FSNDM (*N*,*N*-dimethyl), FSNDE (*N*,*N*-diethyl), and FSNP (*N*-pyrrolidinyl)—paired with LiFSI weakened Li^+–solvent interactions, increased Li^+–anion coordination, and raised the fraction of compact clusters. The resulting salt-derived inner/solvent-derived outer, dense bilayer SEI/CEI combined modest viscosity with decent conductivity (1.6–6.1 mS cm^{-1}). Under ultralow electrolyte dosage (3 g Ah^{-1}) and high-loading NMC811, the FSNDM electrolyte enabled a 6 Ah pouch to cycle stably at 495.5 Wh kg^{-1} for 150 cycles, with high coulombic efficiency (99.71%) in both full and anode-free cells.[49]

Takeaway: molecular engineering that yields "weak coordination + anion enrichment + cluster densification" enables fast, inorganic-rich interphase formation and low-resistance charge transfer—without severely compromising bulk viscosity/conductivity.

Salt species and concentration engineering reshapes coordination statistics and the packing density of ionic clusters, thereby governing interfacial reactions and transport. At the ultra-high-concentration limit, LiFSI (≈16 M) produces a compressed solvation regime in which anion-rich, small-size, high-coordination-density clusters form concurrently at the primary solvation shell and mesoscale. This environment triggers preferential, collective reduction of FSI^-, rapidly constructing a dense, inorganic-rich SEI that is compatible with high-loading cathodes and lean-electrolyte (low E/C) operation.[24]

In contrast to the "HCEs" paradigm, Zhang *et al.* molecularly engineered a low-concentration phosphate-based electrolyte (LCE) that is intrinsically non-flammable and simultaneously stabilized both a high-Ni cathode ($LiNi_{0.9}Co_{0.05}Mn_{0.05}O_2$, NCM9055) and a Li-metal anode. The electrolyte consisted solely of 0.7 M LiDFOB (lithium difluoro(oxalato)borate) dissolved in TMP (trimethyl phosphate). By tailoring anion–solvent interactions, the formulation established an anion-rich solvation sheath even at low salt content (Fig. 2d). Raman spectroscopy and MD simulations confirmed a high fraction of AGG (Fig. 2e and f), which drove preferential $DFOB^-$ decomposition to form LiF- and boron-oxide-rich interphases at both electrodes. Practically, the chemistry sustained stable cycling over −20–60 °C (>180 cycles), raised the thermal runaway onset (158 °C *vs.* 140 °C), dramatically improved high-temperature charged retention (95.1% *vs.* ≈0%), suppressed gas evolution, and achieved 533.8 Wh kg^{-1} in a 20.0 Ah pouch cell.[47]

Bridging these extremes, a locally moderate-concentration electrolyte (LMCE) strategy employs a non-coordinating diluent, fluorobenzene (FB), to dilute a medium-concentration LiTFSI/FEC electrolyte (0.5–1.5 M) down to a total salt content of 0.1 M. Although FB does not enter the Li^+ primary solvation shell, the dilution rebalances Li^+–solvent *vs.* Li^+–anion coordination to yield ordered, moderately sized anionic clusters. Such clusters retain sufficient anion participation to generate a LiF-rich, dense SEI while avoiding over-aggregation that would impede Li^+ transport, thereby enabling a high Li^+ transference number (t_+ = 0.64), low desolvation barriers, and fast interfacial kinetics. The LMCE delivers high-rate, long-life performance across systems including NCM811||Li and anode-free configurations.[50]

A growing body of research highlights the pivotal role played by diluent polarity, dielectric tuning, and field matching in next-generation 500 Wh kg^{-1}-class pouch cells. In typical LHCEs, Zhang *et al.* systematically demonstrated that the dipole moment of diluents critically governs the degree of

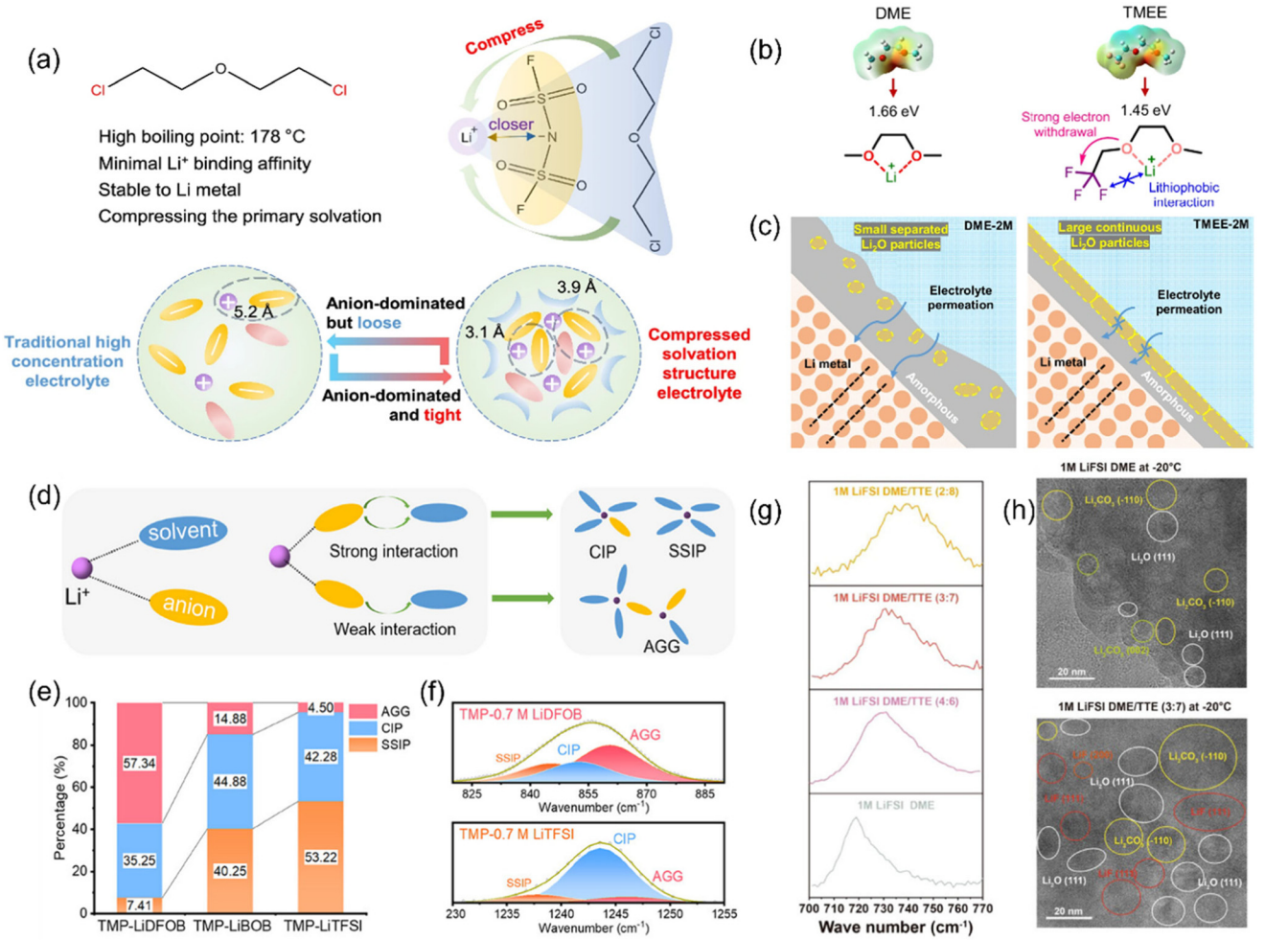

Fig. 2 (a) Molecular characteristics of ClDEE. ClDEE tightly adheres to the outer layer of Li's primary solvation shell, compressing the Li^+–and first source–anions; compared with traditional concentrated electrolytes that are rich in anions but structurally loose, the compressed solvation structure electrolyte has a denser and smaller solvation cluster.[24] (b) Chemical structure design, electrostatic potential and associated properties of DM/TMEE.[34] (c) Schematic illustration of the observed SEIs structures in DME and TMEE electrolytes.[34] (d) Illustration of Li solvation structure resulting from the competition between Li–solvent and Li–anion interactions in LCE.[47] (e) Percentage of solvation structures in three TMP-based electrolytes from the MD simulation.[47] (f) Fitted Raman spectra of TMP-0.7 M LiDFOB and TMP-0.7 M LiTFSI electrolytes.[47] (g) Raman spectra of 1 M LiFSI DME/TTE electrolytes; the increased content of TTE leads to progressive shift of the S–N–S bending peak of FSI^- to a high wavenumber, indicating that more FSI^- participate in the Li solvation shell.[48] (h) Cryo-TEM image of the Li deposited in 1 M LiFSI DME and in 1 M LiFSI DME/TTE (3 : 7) electrolyte.[48]

Li^+–anion aggregation. Specifically, high-dipole, weakly coordinating diluents can effectively exclude coordinating solvents such as DME from the Li^+ primary solvation shell, thus increasing the likelihood of FSI^- entering the inner coordination environment. This facilitates the formation of high-density CIP and AGG, with the CIP + AGG fraction approaching 95%. In lean-electrolyte, high-rate conditions, this design enables 1500 cycles at 10 C, or the 403 Wh kg^{-1} specific energy in pouch cell.[51]

Building on this concept, Xiao *et al.* enhanced the proportion of TTE (1,1,2,2-tetrafluoroethyl-2,2,3,3-tetrafluoropropyl ether)—a low-polarity, non-coordinating diluent—to formulate a wide-temperature electrolyte (WTAE: 1 M LiFSI + 0.02 M $LiNO_3$ in DME : TTE = 3 : 7). This effectively shifted the solvation environment from solvent-dominated to anion-dominated, enabling the formation of LiF-rich interphases and facilitating low-temperature desolvation kinetics across a wide temperature window (−40 °C to 60 °C). As a result, 5.8 Ah pouch cells achieved 503.3 Wh kg^{-1} at 25 °C over 260 stable cycles, and 339 Wh kg^{-1} even at −40 °C.[48] Spectroscopic analysis (Raman, NMR) and molecular dynamics (MD) simulations confirmed enhanced FSI^- coordination and shortened Li^+–Li^+ distances, while cryo-TEM/X-ray Photoelectron Spectroscopy (XPS) directly visualized LiF deposition and F/S–O signal persistence deep within the SEI (Fig. 2g and h).

To further refine interface control, Zhang *et al.* proposed a dielectric-mediated design strategy using solvents like 1,1,1,3,3-pentafluorobutane (PFB). This approach balances

external electric fields and molecular dielectric response, thereby maintaining tight interfacial Li^+–anion coordination, suppressing anion depletion, and limiting parasitic reactions. A 6 Ah pouch cell formulated with this strategy delivered nearly 500 Wh kg^{-1} under E/C = 1 g Ah^{-1} conditions.[52]

Beyond regulating desolvation kinetics and interphase chemistry, the polarity and dielectric response of diluents also exert an important influence on system-level thermal safety. In LHCE-type systems, low-polarity or weakly coordinating diluents can reduce the fraction of free solvent and promote anion-enriched coordination, thereby favoring the formation of dense inorganic-rich SEI/CEI layers and suppressing continuous parasitic reactions at both electrodes. From a thermal perspective, such effects are beneficial because they decrease the availability of flammable/reactive solvent species, mitigate gas evolution, and reduce cathode-side exothermic degradation under highly charged states. Therefore, the thermal runaway onset temperature is not dictated by dielectric constant alone; rather, diluent polarity and dielectric response affect it indirectly through the coupled regulation of combustibility/volatility, Li^+ solvation structure, interphase chemistry, and electrode–electrolyte side reactions. This explains why dielectric-tuned systems such as TMP-, TTE-, and PFB-containing electrolytes can simultaneously improve interfacial stability and enhance abuse tolerance in practical high-energy pouch cells.

Zhang *et al.* advanced a fluorinated hybrid diluent modulation strategy, in which a LiFSI/DEE-based electrolyte was formulated with a mixture of low-polarity TTE (inert diluent) and sacrificially decomposable BTFE (bis(trifluoroethyl) difluoroethane).[53] This hybrid diluent (LHCE-TB) reorganized the ionic cluster structure, as confirmed by MD simulations and spectroscopic analyses, yielding smaller and more dynamic AGGs and shifting Li^+ transport from solvent-carried migration to a more efficient structural diffusion mechanism. Meanwhile, BTFE co-decomposed with FSI^- to form thin LiF-rich inorganic SEI/CEI layers, simultaneously ensuring wide-temperature operation and high-voltage stability. In practical demonstrations, a 5.81 Ah NCM9055‖Li pouch cell (≈25 mg cm^{-2} loading, 50 μm Li, E/C = 1.4 g Ah^{-1}) delivered 508.5 Wh kg^{-1} at 25 °C and ≈457.6 Wh kg^{-1} at −20 °C, highlighting the promise of molecularly engineered diluents to synergistically optimize low-temperature ion transport and interfacial passivation.

By contrast, Peng *et al.* developed a functional-divided hybrid diluent (C-DHCE) combining fluorinated aromatics (FB/F_3B) and TTE: the aromatics facilitated Li^+ desolvation and transport, whereas TTE ensured oxidative tolerance and interfacial stability. This cooperative design reorganized solvation and mesoscale clusters, forming inorganic-rich SEI/CEI and enabling a 2.95 Ah NCM811‖Li pouch cell (E/C = 3 g Ah^{-1}) to deliver ≈518 Wh kg^{-1} (≈985 Wh L^{-1}) with stable cycling beyond 100 cycles.[54] While Zhang *et al.* emphasized sacrificial decomposition for interphase construction, Peng *et al.* achieved dual optimization of kinetics and interfacial robustness through functional division—together underscoring the pivotal role played by hybrid diluents in advancing wide-temperature, high-energy-density LMBs.[53,54]

In a parallel advance, Jie *et al.* introduced the concept of Compact Ion-Pair Aggregates (CIPAs), deliberately engineered to form nanometer-scale (3–4 nm), densely packed Li^+–anion clusters—significantly larger and structurally more compact than the typical ∼1 nm clusters in LHCEs. A representative CIPA electrolyte (2 M LiFSI in ethylene glycol di-*n*-butyl ether (EGBE) and TTE, 1 : 1) yielded Li^+–Li^+ spacings ≈6 Å, enabling collective interfacial electron transfer and rapid generation of thin, inorganic-rich SEI layers. Under E/C = 1.25 g Ah^{-1} with a high-Ni cathode, the electrolyte enabled an energy density of approximately 505.9 Wh kg^{-1} while maintaining a stability of 91% for 130 cycles and further boosted to approximately 520.3 Wh kg^{-1} (95% stability for 100 cycles) at a cutoff voltage of 4.4 V.[55]

Recently, Huang *et al.* introduced the concept of a delocalized electrolyte (UDE), in which multi-solvent and multi-diluent combinations are employed to construct a high configurational entropy (S_{config}) solvation environment.[56] This disperses the Li^+ primary solvation shell, thereby reducing desolvation barriers and enhancing ion transport. The resulting interphases are enriched with LiF, Li_3N, and Li_3SO_x, suppressing parasitic reactions and dendrite growth. In practical demonstrations, a 5.5 Ah Ni90‖Li pouch cell (E/C = 1.0 g Ah^{-1}) achieved 604.2 Wh kg^{-1}, while a 5.2 Ah pouch cell under ultra-lean conditions (E/C = 0.9 g Ah^{-1}) delivered 618.2 Wh kg^{-1}; even a 3.9 kWh battery pack maintained 480.9 Wh kg^{-1} with enhanced safety. This study highlights how solvent/diluent engineering toward delocalized solvation can enable ultrahigh-energy-density lithium metal batteries.

Most recently, weak-coordination fluorinated-solvent design has been pushed into the hydrofluorocarbon regime, yielding a new benchmark for ultra-high-energy-density lithium-metal pouch cells. Wu *et al.* reported a monofluorinated hydrofluorocarbon electrolyte based on 1.13 M LiFSI/DFP, in which weak F–Li^+ coordination, low viscosity, high oxidative stability, and exceptionally high wettability were jointly realized.[57] The resulting electrolyte delivered high Li‖Cu reversibility (up to 99.7% CE) and enabled stable operation over a wide temperature range, while the high wettability of DFP was found to be particularly important for achieving lean-electrolyte pouch cells. In practical demonstrations, 13.33 Ah Li‖Ni96 pouch cells with 33.5 mg cm^{-2} cathode loading, 20 μm Li, and E/C ratios of 0.48–0.56 g Ah^{-1} achieved 701–707 Wh kg^{-1}, whereas Li‖NMC811 pouch cells also reached 563–606 Wh kg^{-1} under more balanced cathode chemistry. This work further highlights how low-coordination, high-wettability solvent design can simultaneously address desolvation kinetics, high-voltage compatibility, and practical pouch-level energy density in lean-electrolyte LMBs.

In summary, a synergistic triad of weak coordination/terminal-group engineering, salt species/concentration optimization, and dielectric-matched diluent selection collectively advances a unified mechanistic pathway: "compressed primary solvation shell → dense ion clusters → preferential anion reduction → inorganic-rich SEI/CEI". Beyond enabling long cycle life and fast interfacial kinetics, this pathway also con-

tributes to wider-temperature operability and improved thermal safety by reducing free-solvent activity, suppressing gas-evolving side reactions, and stabilizing both electrode interfaces under practical conditions.

2.2 Functional additives

Once the primary electrolyte matrix—including solvent, salt, and diluent—has been established, functional additives offer a low-cost, easily tunable means to refine the sequence of decomposition, guide the composition and origin of interphase components, and locally tailor the solvation structure and ionic cluster density, all without significantly altering the bulk viscosity or transport properties. These additives serve as targeted enhancers for specific performance limitations such as high-voltage endurance, wide-temperature operability, or fast-charging capability. Compared to solvent/salt/diluent engineering, additives provide higher selectivity, and when integrated with section 2.1 strategies, they can deliver more robust performance in practical windows—namely, lean electrolyte (low E/C), thin lithium metal anodes, and high cathode areal loadings.

Tang *et al.* proposed a ternary additive strategy for carbonate-based, high-voltage LMB electrolytes, comprising fluoroethylene carbonate (FEC), cetyltrimethylammonium chloride (CTAC), and tris(pentafluorophenyl)borane (TPFPB). Here, FEC promotes the formation of fluorine-rich, dense, and chemically stable SEI/CEI, while CTAC, acting as a surfactant, modulates the interfacial Li^+ solvation environment and deposition kinetics. TPFPB contributes to improved mechanical integrity and ionic conductivity of the interphase. It can be clearly observed from the scanning electron microscopy (SEM)/transmission electron microscopy (TEM) images of the positive and negative electrode surfaces that the combined effect of the three elements results in the formation of dense and highly ion-conductive interface films on both the positive and negative electrode surfaces, effectively inhibiting dendrite growth and high-voltage oxidative decomposition (Fig. 3a and b). Through testing, benefiting from a superior interface layer, ternary composite additives exhibit better ionic conductivity, higher exchange current, and a wider electrochemical stability window compared to binary additives or the blank group (Fig. 3c). Under thin-Li and high-loading cathode conditions, the resulting pouch cells reached a specific energy of 522 Wh kg^{-1} with a capacity retention of 80.9% over 178 cycles.[58]

Aiming for ultra-high-voltage stability, Liu *et al.* employed a partially fluorinated electrolyte (FEC/EMC) in combination with a novel additive, trimethylsilyl borate (TMSB), to co-modulate the interfacial solvation structure and construct a highly stable "armored" CEI. FEC facilitated the formation of a LiF-enriched inner layer, while the decomposition products of TMSB formed an inorganic-rich outer layer with high Li^+ conductivity and the ability to suppress lattice oxygen release. Together, these interfacial features yielded excellent mechanical and electrochemical stability. Even at 4.9 V cutoff, a 9 Ah pouch cell retained high interfacial integrity and achieved an energy density of 576 Wh kg^{-1} with superior cycling performance.[59]

To selectively manipulate anion chemistry, Hao *et al.* introduced an anion-sieving coordination strategy, using *N*-methylbis(trifluoroacetamide) (MBTFA) as an additive in a dual-salt electrolyte system comprising $LiBF_4$/LiDFOB. MBTFA promoted preferential coordination of $DFOB^-$ anions over BF_4^-, the latter being less favorable for SEI/CEI formation. This strategy enriched the solvation environment with $DFOB^-$, thereby guiding the decomposition process toward the formation of a B/F-rich inorganic CEI with enhanced mechanical robustness. The optimized interfacial chemistry effectively mitigated electrolyte decomposition and cathode structural degradation under high voltage. Full cells with Li‖NCM811 configuration operated at 4.7 V, 55 °C, and low electrolyte loading (0.95 g Ah^{-1}), achieving a remarkable energy density of 541 Wh kg^{-1} with outstanding cycling stability.[60]

Building on these additive strategies, researchers have also begun to explore synergistic regulation between additives and salts. For example, Liu *et al.* reported a design based on a $LiBF_4$ electrolyte combined with the functional additive *para*-fluorobenzeneacetonitrile (*p*-FBCN). Owing to its preferential decomposition, *p*-FBCN directed the formation of a "sandwich-model" cathode–electrolyte interphase (CEI), comprising an inner LiF-rich inorganic layer and an outer P–N–F covalent network. This dual-layer CEI simultaneously suppressed electrolyte oxidation and lattice oxygen release under high voltage while maintaining high Li^+ conductivity. The strategy significantly enhanced the stability of Li‖NCM94 (|$LiNi_{0.94}Co_{0.05}Mn_{0.01}O_2$) cells under both high-voltage and wide-temperature conditions, and in a 7.6 Ah pouch cell achieved ≈544 Wh kg^{-1} energy density with durable cycling.[26] This work underscores the role played by functional additives in controlling decomposition sequences and guiding interfacial composition, while demonstrating a promising "salt–additive synergy" pathway for high-energy-density, all-climate lithium metal batteries.

In summary, functional additives complement the strategies in section 2.1 by offering selective tuning of interfacial chemistry through modifying precursor composition, decomposition order, and local complexation/weak coordination environments. Beyond stabilizing Li-metal deposition, these mechanisms are equally important for suppressing electrolyte oxidation, mitigating lattice-oxygen release, and constructing mechanically robust, ion-conductive CEI layers at high-voltage cathodes. As such, additive engineering should be viewed not only as an anode-protection strategy, but also as a critical route to improve cathode-side oxidative stability in practical high-energy LMBs.

2.3 Interfacial functional materials

Even with well-optimized bulk electrolytes and functional additives, the solid–liquid interfacial chemistry and morphology remain dominant factors determining failure modes and cycle life, especially under challenging conditions such as thin lithium metal anodes and lean electrolyte (low E/C) operation. As a complementary strategy, interfacial functional materials have emerged as a third critical design dimension. These

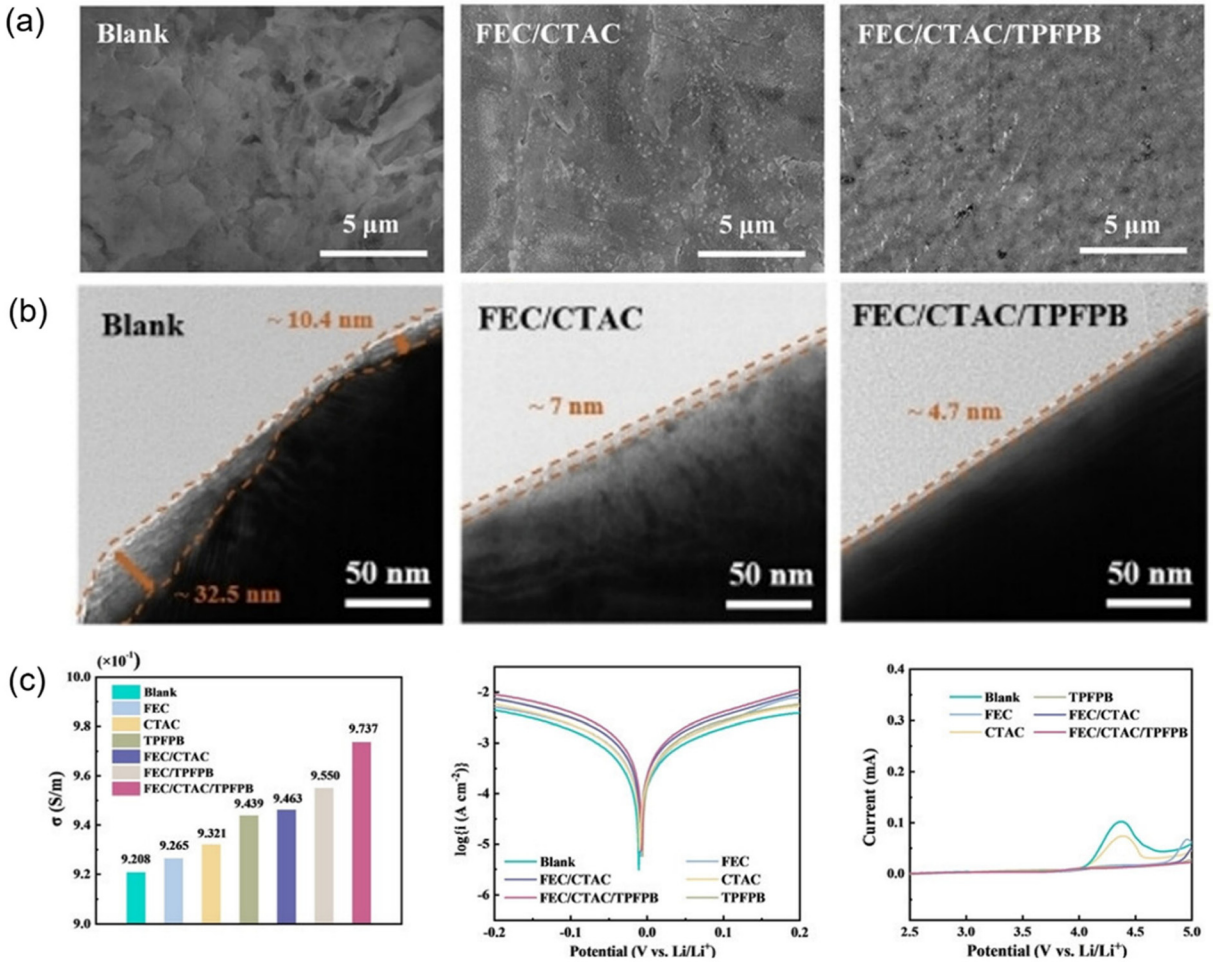

Fig. 3 (a) Top-view SEM images of Li anode at 1 mA cm^{-2}/3 mAh cm^{-2} after 10 cycles within blank electrolyte, FEC/CTAC-containing electrolytes and FEC/CTAC/TPFPB-containing electrolytes. (b) TEM images of LNMO cathode particles cycled within blank electrolyte, FEC/CTAC-containing electrolytes and FEC/CTAC/TPFPB-containing electrolytes. (c) Ionic conductivity/Tafel curves of Li|Li symmetric cells/LSV curves of the Li–aluminum (Al) cells of electrolytes with different additives.[58]

materials operate independently of bulk formulations, aiming to reduce nucleation overpotential, suppress side reactions, and guide uniform Li deposition *via* a combination of: (i) low-tortuosity, ion-selective transport geometries, (ii) localized solvation structure and cluster reorganization, (iii) programmable precursor delivery. In doing so, they can synergistically reinforce the benefits of electrolyte-based strategies and further extend operational windows for high-energy LMBs.

Recent studies have demonstrated that interfacial functional materials can indirectly modulate Li^+ solvation structure and transport dynamics. For example, a macroscopically uniform, grain-boundary-free artificial interlayer was constructed using protonated graphitic carbon nitride (PCN) nanosheets and polyethylene oxide (PEO) as a composite structure coated on the lithium-metal surface.[25] The PCN nanosheets offer in-plane ordered porosity and abundant nitrogen coordination sites, which enable low-tortuosity, selective Li^+ transport pathways. Their weak Li^+ coordination also modifies the local solvation sheath, promoting easier Li^+ desolvation and metal incorporation at the interface, thus improving the uniformity of deposition (Fig. 4a). COMSOL simulations together with SEM of Li deposition reveal that, on a rough Cu-foil model, the current density preferentially concentrates in the concave regions, indicating that Li on the PCN–PEO@Cu electrode tends to deposit in these recesses rather than at foil tips (Fig. 4b and c). SEM images of the plated electrodes further confirm that Li nuclei are uniformly distributed beneath the robust PCN–PEO interlayer, and no dendritic crystals are observed on PCN–PEO@Cu (Fig. 4d and e). Higher-magnification SEM (inset) shows hexagonal single-crystal Li domains (~200 nm), which are attributed to the high interfacial Li-transport rate.[36] These results indicate that a Li-selective interface promotes favorable nucleation and, in turn, induces uniform Li deposition. PEO, with its high Li^+ conductivity, facilitates rapid and stable Li^+ transfer across the interface. This composite interlayer not only suppressed dendrite growth and parasitic reactions but also enabled stable cycling in current-collector-free (CC-free) Li anode systems. In pouch

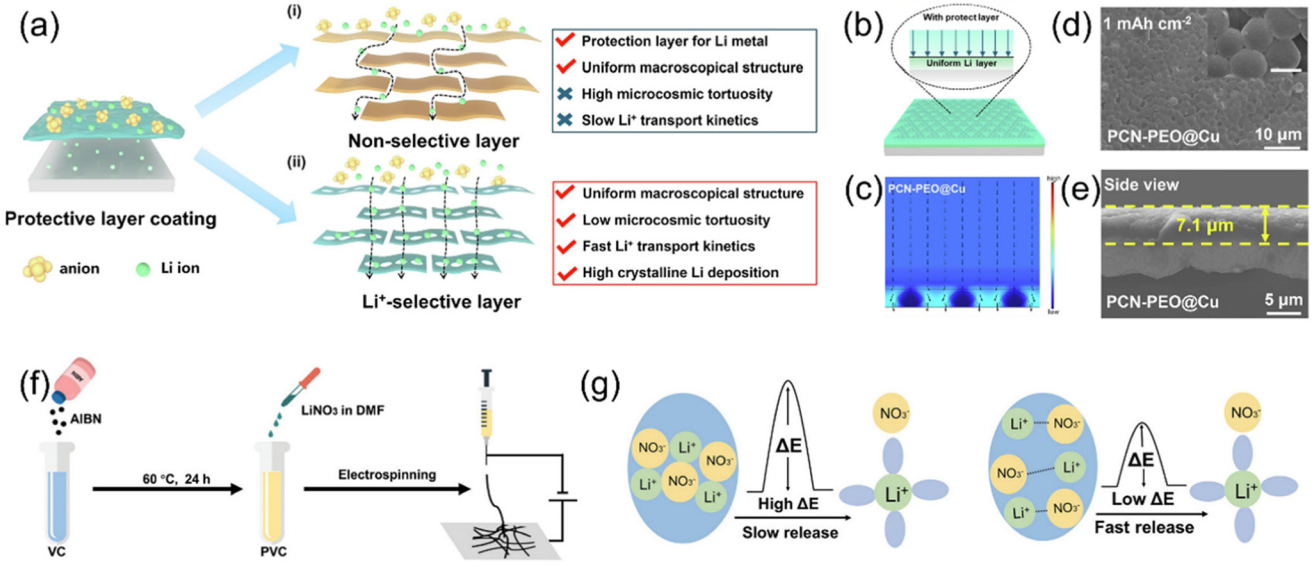

Fig. 4 (a) 2D material's protective layer coating on Li metal by (i) common 2D materials; (ii) Li-selective conduction 2D materials.[25] (b) Schematic illustration of Li plating behaviors of PCN–PEO@Cu.[25] (c) COMSOL simulations of current density for PCN–PEO@Cu.[25] SEM characterization studies of (d) top view and (e) side view after Li plating at 0.5 mA cm^{-2} for 1 mAh cm^{-2}; the scale bar of inner image was 200 nm.[25] (f) Preparation of LNO–PVC intermediate layer by electrospinning.[61] (g) Crystalline $LiNO_3$ with a high activation energy and slow $LiNO_3$-release. Dissociated $LiNO_3$ with a low activation energy and fast $LiNO_3$-release.[61]

cell configurations, the PCN–PEO interlayer enabled a 324 Wh kg^{-1} cell to retain 90.0% capacity after 300 cycles with an average coulombic efficiency of 99.7%. In the CC-free configuration, the energy density increased to 506 Wh kg^{-1}, with stable operation for 160 cycles.

Within the category of artificial interphases, Jiang *et al.* reported a molecular surface reconstruction strategy, in which a perfluoro(2-methyl-3-oxahexanoic) acid (PFOA) solution was sprayed onto lithium metal to form a PFOA–Li precursor layer that subsequently evolved through sequential chemical–electrochemical reactions into a multilayer SEI enriched with LiF/Li_2O nanocrystals.[62] The hetero-grain boundaries provided fast Li^+ transport channels while the inorganic-rich SEI exhibited a high mechanical modulus (≈5.56 GPa), effectively mitigating interfacial stress and dendrite growth. Electrochemical analysis revealed an increased Li^+ transference number (from 0.28 to ≈0.51) and suppression of dead Li/LiH accumulation. Importantly, in engineering-scale tests, a 5.8 Ah NCM90||Li pouch cell (≈39.6 mg cm^{-2} loading, 100 μm Li, E/C = 1.12 g Ah^{-1}) achieved 518 Wh kg^{-1} energy density with stable cycling over 100 cycles. This work highlights interphase reconstruction as an effective pathway to combine high ionic conductivity with mechanical robustness, thereby advancing practical high-energy-density lithium metal batteries.

Another research study employed 2,2-difluoro-2-(fluorosulfonyl)acetic acid (DFFSA) as a precursor to construct a multicomponent, gradient artificial SEI *via in situ* spraying. This approach enabled the formation of distinct inner and outer functional layers, significantly reducing interfacial resistance and effectively suppressing Li dendrite growth. The resulting interphase substantially enhanced Li metal stability, enabling long-term cycling in pouch cells with energy density approaching 500 Wh kg^{-1} (461.6 Wh kg^{-1}).[63]

In addition to geometric and chemical control, salt-embedded interlayers have recently emerged as a promising approach for delivering interfacial functionality *via in situ* release mechanisms. Yang *et al.* developed an electrospun interlayer composed of poly (vinylene carbonate) (PVC) and dissociated-state $LiNO_3$ (LNO–PVC interlayer, Fig. 4f), enabling programmable additive delivery at the Li metal interface without altering the bulk electrolyte formulation.[61] Unlike conventional $LiNO_3$ additives, which suffer from low solubility and sluggish diffusion in carbonate electrolytes, this design pre-dissolves $LiNO_3$ in DMF before electrospinning with PVC, yielding a 3D porous membrane where $LiNO_3$ exists in a non-crystalline, ionically dissociated form. Upon cycling, this structure allows for rapid and sustained release of active $LiNO_3$ into the interfacial region (Fig. 4g), inducing the formation of a robust SEI rich in Li_3N and LiF, and enhancing interfacial transport kinetics. Structural and spectroscopic analyses (XRD, FTIR, XPS) confirmed the dissociated salt state and preferential formation of inorganic SEI species, while electrochemical tests showed substantial improvements: average coulombic efficiency of 98.6% in Li–Cu cells, over 1000 h lifetime in symmetric Li–Li cells, and a 400 Wh kg^{-1} soft-pack Li||NCM811 pouch cell with stable cycling over 65 cycles. This work introduces a novel "salt-in-interlayer" strategy that decouples additive functionality from bulk electrolyte solubility constraints, achieving spatially localized additive delivery and targeted interphase formation—a scalable and effective pathway to stabilize Li metal interfaces under high-voltage, lean-electrolyte conditions.

In another innovative work, Ji *et al.* proposed a micro-emulsion electrolyte strategy for interfacial regulation.[64] In a car-

bonate-based electrolyte (1.0 M LiDFOB + 0.2 M $LiBF_4$ in DEC : FEC), an immiscible perfluorinated compound, PFP (1,1,1,2,2,4,5,5,5-nonafluoro-4-(trifluoromethyl)-3-pentanone, IM-F), was introduced together with a partially fluorinated ether, TTE (1,1,2,2-tetrafluoroethyl-2,2,3,3-tetrafluoropropyl ether, AM-F), acting as a surfactant to form stable IM-F@AM-F micelles (50–120 nm). Driven by liquid–liquid interfacial tension (γL–L), these micelles spontaneously migrate and enrich at both lithium anode and high-Ni cathode interfaces, inducing the formation of thin, inorganic-rich SEI/CEI layers dominated by LiF and Li_3N. A suite of characterization studies (cryo-EM, Raman, XPS, ToF-SIMS) confirmed this interfacial delivery and robust interphase formation. In pouch cell demonstrations, a 7.2 Ah Ni90||Li cell (E/C = 1.0 g Ah^{-1}) delivered 531 Wh kg^{-1} with 81% retention after 189 cycles, while a 7.5 Ah pouch cell still achieved 547 Wh kg^{-1} and 79% retention after 155 cycles under more demanding conditions. This study leveraged liquid–liquid interfacial tension as a driving force for the active delivery of interfacial functional materials, transforming static coatings into mobile precursors within the electrolyte, thereby offering a new pathway toward practical high-energy-density lithium metal batteries.

Beyond these programmable interfacial strategies enabled by salt-embedded interlayers or liquid-phase delivery, researchers have also explored precursor design to achieve more ordered interphase formation. The "sequential reaction" approach proposed by Liu *et al.* exemplifies this concept, using a pre-coated layer to guide stepwise chemical and electrochemical reactions and thereby constructing a structured, multilayer SEI on the lithium metal surface, in which a sulfurized polyethylenimine (SPEI) precursor layer was pre-coated onto the lithium metal surface to enable an ordered film-formation process.[65] Specifically, SPEI first chemically reacted with Li to form a dense and uniform Li_2S inner layer, which was subsequently converted during cycling into a Li_2S/Li_3N intermediate layer, while the outer organic SPEI remained as an elastic buffer. This multilayer SEI structure provided both fast Li^+ transport channels and mechanical compliance to mitigate stress and suppress crack formation and dendritic growth. Characterization studies including cryo-TEM, ToF-SIMS, and DFT confirmed the compositional gradients and ion-transport advantages of the layered SEI. Under near-practical conditions (NCM811 cathode with 6.0 mAh cm^{-2} areal loading and E/C = 1.35 g Ah^{-1}), a 3.4 Ah pouch cell delivered an energy density of ≈480.5 Wh kg^{-1} with 85.9% capacity retention after 100 cycles.

Unlike the bulk-centered approaches in sections 2.1 and 2.2, interfacial functional materials offer "dual selectivity"—geometric and chemical—targeting Li^+ transport pathways and interfacial reaction kinetics. As such, they are essential to pushing the practical performance boundaries of high-loading, thin-Li, low-E/C battery systems.

2.4 Effects of novel salts

While the regulation of solvation structures and ionic clusters primarily relies on solvent chemistry, salt species play an equally decisive role in dictating electrolyte properties, interphase composition, and long-term cell stability. The choice and design of lithium salts not only determine the ionic dissociation degree, Li^+ transport kinetics, and electrochemical stability window, but also influence the preferential decomposition pathways that shape SEI/CEI chemistry. Beyond serving as the primary lithium source, novel salts together with functional salt additives such as Na^+-based compounds can synergistically modulate Li^+ coordination environments, enrich inorganic interphase components, and suppress parasitic reactions at both electrodes. Such salt-centric strategies, often working in concert with solvent and additive engineering, have emerged as a powerful toolset for enabling high-energy-density, safe, and durable LMBs under practical operating conditions.

Xia *et al.* introduced a novel asymmetric ether-chain lithium salt (LiFEA) (Fig. 5a), designed to possess a crown-ether-like folded conformation, high dipole moment, and elevated donor number (DN). LiFEA not only enhanced the Li^+ transference number but also endowed carbonate-based electrolytes with a "self-cleaning" capability—dissolving organic by-products in the SEI and promoting inorganic enrichment—thus generating dense, uniform, LiF/Li_2O-rich interphases (Fig. 5b). Furthermore, LiFEA improved the solubility and utilization of $LiNO_3$ additives in carbonate systems, achieving synergistic interphase stabilization on both Li metal and high-voltage NCM811 cathodes. Pouch cells demonstrated high energy (310 Wh kg^{-1}) and power density (410 W kg^{-1}) with excellent fast-charging capability and extended cycle life.[27] This work highlights how molecular-level design of new lithium salts can simultaneously regulate solvation chemistry and interfacial reactions, yielding performance gains unattainable by conventional salts.

To address the limitations of $LiPF_6$—including thermal/electrochemical instability, hydrogen fluoride (HF) generation, and interfacial degradation under high-temperature/high-voltage conditions—recent research has turned to anion chemistry engineering in main lithium salts. Chen *et al.* reported a highly fluorinated lithium borate salt (LiFPB) that combines robust covalent C–F bonds with functional borate moieties (Fig. 5c), eliminating HF formation at the source and forming LiB_xO_y-rich fast-ion-conducting SEI on the anode and organic/inorganic composite CEI on the cathode. This dual stabilization suppresses dendrites and preserves high-voltage cathode structure, enabling LCO/Li (50 μm Li) cells to retain 80% capacity after 260 cycles at 60 °C and 4.45 V, with stable operation even at 100 °C.[66] Qiao *et al.* developed a non-corrosive hydrogenated sulfonimide salt (LiDFTFSI) by introducing $-CHF_2$ groups into the anion, destabilizing $Al(DFTFSI)_3$ in carbonate solvents and promoting its decomposition into insoluble AlF_3/LiF layers that protect the Al current collector while maintaining a 5.6 V electrochemical stability window and 90-day chemical stability.[68] Mandouma *et al.* presented the weakly coordinating anion/cation salt TAPOMe/TFAB, in which bulky tetra-*p*-methoxyphenylphosphonium cations and tetrakis(pentafluorophenyl)borate anions—with electron-donating $-OCH_3$ substituents—reduce the ion-pair association

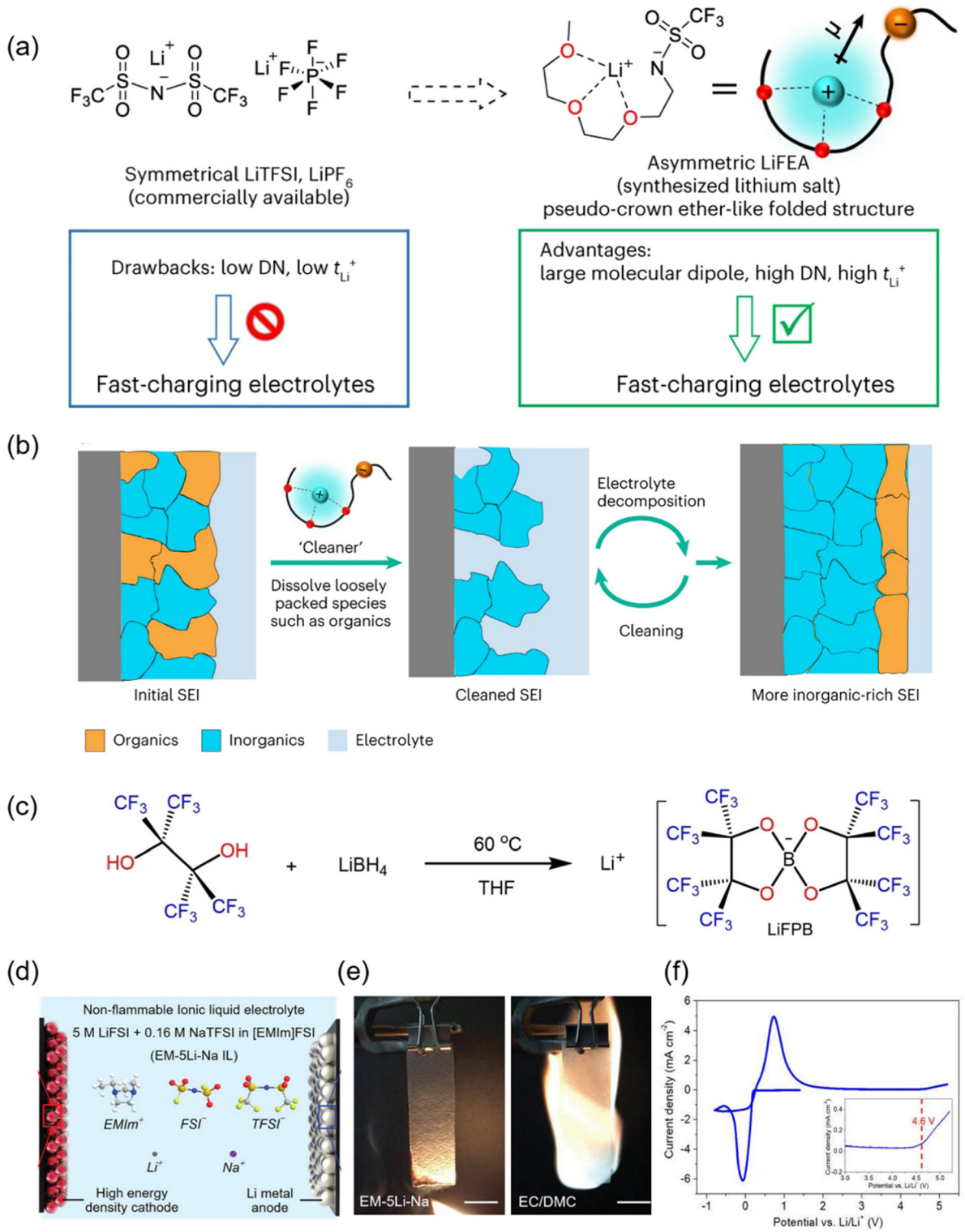

Fig. 5 (a) Chemical structures and drawbacks/advantages of commercial, symmetrical Li salts and LiFEA with a pseudo-crown ether-like folded structure in carbonate electrolytes.[27] (b) The proposal for self-cleaning of the SEI mechanism.[27] (c) Synthetic route of LiFPB salt.[66] (d) Schematic illustration of the electrolyte composition of the EM-5Li-Na IL electrolyte.[67] (e) Flammability tests of the EM-5Li-Na IL electrolyte and conventional organic electrolyte consisting of 1 m $LiPF_6$ in EC/DMC (1 : 1 by vol).[67] (f) Linear sweep voltammetry profile of a Li–Al cell using EM-5Li-Na IL electrolyte.[67]

constant (K_a = 3.3 × 10^3 M^{-1}), delivering tetrabutylammonium hexafluorophosphate (TBA–PF_6)-comparable molar conductivity (78.6 S mol^{-1}) in low-polarity solvents (THF, TBME) and opening electrolyte options for unconventional high-energy systems.[69] Collectively, these cases demonstrate that enhancing thermal stability, expanding the electrochemical window, and optimizing solvation structure *via* molecular design is critical for advancing practical >500 Wh kg^{-1} LMBs.

Unlike main salts that define bulk electrolyte properties, functional salt additives are used in small amounts to preferentially participate in initial interfacial reactions, tailoring SEI/CEI composition and architecture for improved cycling stability and rate performance. Sun *et al.* developed a nonflammable ionic-liquid-based electrolyte (EM-5Li-Na) combining LiFSI with sodium bis(trifluoromethanesulfonyl)imide (NaTFSI) as a functional co-salt (Fig. 5d). The incorporation of Na^+ ions modified Li deposition behavior, suppressing dendrite growth and enabling uniform plating, while the FSI^- anions preferentially decomposed to form dense, inorganic-rich SEI/CEI layers. The ionic liquid matrix further contributed intrinsic nonflammability and a wide electrochemical stability window (Fig. 5e and f). As a result, Li||NCM811 pouch cells delivered energy densities exceeding 765 Wh kg^{-1} with prolonged cycling stability and improved thermal safety. This work demonstrates the efficacy of co-salt engineering—here *via* NaFSI—as a multifunctional salt additive strategy for safe and high-energy LMBs.[67]

The co-salt strategy has shown considerable application potential in LMBs leading to significant progress in lithium metal protection and the development of high-performance LMBs. Studies have demonstrated that introducing LiFSI as a co-salt into an electrolyte based on LiTFSI can markedly enhance coulombic efficiency and effectively suppress dendrite formation at a high current density of 10 mA cm^{-2}, owing to the higher reactivity of the FSI^- anion, which preferentially forms a LiF-rich SEI.[70] Qiu *et al.* reported a concentrated mixed-salt electrolyte composed of LiTFSI/LiFSI co-salts with lithium nitrate ($LiNO_3$) as an additive, where LiFSI promotes LiF formation and $LiNO_3$ facilitates Li_2O formation, working synergistically to achieve uniform lithium deposition, while LiTFSI serves to stabilize the highly concentrated electrolyte structure.[71] The most commonly used lithium salts in the co-salt strategy for electrolytes include $LiPF_6$, $LiNO_3$, LiFSI, LiTFSI, LiDFOB, LiBOB and $LiBF_4$,[71–76] whereas novel lithium salts are rarely employed. The main reason is that directly using novel lithium salts as the sole main salt in electrolytes remains challenging.

Son *et al.* introduced the asymmetrically functionalized polar molecule MPS (3-mercapto-1-propanesulfonate sodium), which bears both lithium-affinitive thiol (–SH) and polar sulfonate ($–SO_3^-$) groups, with a high dipole moment of 4.7 D. This enables preferential adsorption at surface defects during Li plating, directing growth along the stable (110) crystal facet and suppressing dendritic tip formation. Its decomposition products enrich the SEI with LiF and Li_2S, combining mechanical robustness with high ionic conductivity. As a result, Li–Li symmetric cells operated stably for over 1200 cycles at 5 mA cm^{-2}.[77] In contrast to the "system-level" optimization of main salts, such additives achieve interface-scale precision engineering through dipole-moment tuning and multifunctional group synergy.

Lithium salts do far more than supply Li^+: through anion/cation chemistry they dictate electrolyte dissociation, solvation motifs, ESW, and the preferential decomposition pathways that define SEI/CEI composition. Molecularly engineered main salts (*e.g.*, highly fluorinated/borate/sulfonimide variants, weakly coordinating ions, bulky cations) suppress HF genesis and Al corrosion, enhance high-voltage stability, and steer interphases toward LiF/Li_2O/Li_3N/$LiBO_x$-rich architectures. Co-salts and functional salt additives (*e.g.*, $LiNO_3$, LiDFOB, Na^+ co-salts, anion receptors) operate at low dosage as sacrificial/targeted formers, synchronizing with solvent/additive engineering to raise Li^+ transference number (t_{Li^+}), curb parasitic reactions, and stabilize both electrodes. Under thin-Li, lean-electrolyte, and high-T/V conditions, salt-centric design provides a scalable route to co-optimize safety, lifetime, and fast-charge capability in practical LMBs.

3. Quasi-solid/polymer electrolytes

3.1 Intermolecular interactions in polymer electrolytes

Intermolecular interactions within polymer electrolytes play a vital role in dictating their electrochemical performance and stability, especially in LMBs targeting high energy densities such as 500 Wh kg^{-1}. Understanding and controlling these interactions are essential for overcoming key challenges, such as limited ionic conductivity, interfacial instability, and dendrite formation associated with lithium metal anodes.

In conventional solid polymer electrolytes (SPEs)—notably those based on polyethylene oxide (PEO)—ionic transport primarily occurs through the segmental motion of the polymer chains. The core driving force at a molecular level is the interaction between polar groups along the polymer backbone (*e.g.*, ether oxygen in PEO) and lithium ions. Lithium ions coordinate with multiple polymer segments, resulting in transient and dynamic solvation sites. This dispersion ensures not only effective conduction pathways but also imparts flexibility to the polymer matrix, enhancing its ability to conform to interfaces with dynamic electrode surfaces and minimizing interfacial resistance.

However, these same ionic interactions must be carefully balanced. Strong coordination between polymer segments and lithium ions, while ensuring ion solvation, also restricts chain mobility, reducing ionic conductivity at ambient temperatures. Likewise, insufficient coordination weakens ion dissociation and transport. To improve conductivity and interfacial compatibility, recent approaches have utilized polymer blending, copolymerization, and the addition of ion-conducting ceramic nanoparticles. These modifications tailor microphase separation and adjust local chain dynamics, thus enabling more facile ion transport.

The intermolecular interactions also critically determine the electrochemical stability of polymer electrolytes, especially under high-voltage operation. While polymers like PEO demonstrate inherent stability and do not easily undergo direct reduction at a lithium metal anode, their performance can be compromised by side reactions triggered by strong interactions between ions, polymer chains, and highly conductive cathode materials at elevated voltages. For example, oxidation of PEO at voltages above 4.2 V can initiate polymer degradation, indicating the influence of molecular-level interactions with both ions and electrode surfaces.

To address these limitations, layered or composite electrolytes that combine polymer flexibility with the mechanical stability of inorganic fillers have been explored. In such systems, molecular-level compatibility, thus desired intermolecular interactions, must be critically engineered at interfaces to support efficient lithium-ion transport while maintaining stability against both lithium metal and high-voltage cathodes.

The precise engineering of intermolecular interactions in polymer electrolytes is key to achieving the ionic mobility, mechanical integrity, and chemical stability demanded by next-generation high-energy-density LMBs. From an application-oriented perspective, one particularly important extension of this concept is the development of composite polymer/inorganic electrolytes, in which intermolecular interactions must be co-optimized not only within the polymer matrix, but also across heterogeneous organic–inorganic domains. Advanced design strategies focus on optimizing such interactions through polymer architecture, functional group incorporation, and hybridization to support safer operation, longer cycling lifespans, and ultimately, the realization of 500 Wh kg^{-1} battery systems.

Building upon the fundamental understanding of intermolecular interactions in polymer electrolytes, recent advancements have increasingly focused on engineering these interactions at the molecular level to optimize both ionic transport and electrochemical stability. One prominent strategy centers around modifying the nature and strength of polymer–ion interactions—particularly in solid polymer electrolytes (SPEs)—to reconcile the inherent trade-off between ionic conductivity and oxidative stability. For instance, the introduction of Lewis-acidic coordination sites within poly(ethylene oxide) (PEO) matrix exemplifies how targeted control of intermolecular forces can propel SPE performance. By doping PEO with Mg^{2+} or Al^{3+} salts, these multivalent cations strongly coordinate with ether oxygen atoms on the polymer backbone (Fig. 6a). This coordination effectively tunes the local electron density and alters the classic ion–polymer interaction landscape: it not only promotes salt dissociation and lithium-ion transport but also suppresses undesirable oxidative decomposition of the polymer. As a result, this molecular-level interaction extends the electrochemical stability window of PEO-based SPEs up to 5 V—well above the traditional ~4.2 V ceiling for neat PEO (Fig. 6b)—facilitating highly stable operation with energy densities approaching 586 Wh kg^{-1} for hundreds of cycles.[28]

Furthermore, strategies such as Zn^{2+}-based ion bridging take the concept of molecular interaction engineering a step further. By forming robust Zn–O bridges within polyether matrices, the polymer's ether linkages are shielded from oxidation, boosting the electrochemical stability window above 5 V and enabling the construction of high-capacity pouch cells with both impressive gravimetric energy (303–452 Wh kg^{-1}) and safety under mechanical abuse.[81]

Beyond tailoring polymer–ion interactions at the molecular level, recent advances also highlight the critical role played by anion design in modulating the intermolecular environment within polymer electrolytes. Rather than focusing exclusively on the polymer matrix, Yan *et al.* adopted an anion-centered strategy by selectively fluorinating aromatic lithium salts (Fig. 6c). This deliberate molecular modification alters the Li^+ solvation structure within PEO polymer matrices, fundamentally reshaping the ion–polymer–anion triplet interactions that govern both ion transport and interfacial chemistry. By tuning the coordinating strength and spatial disposition of the anion, the modified salts facilitate the formation of more robust and stable solid–electrolyte interphases (SEIs) at the lithium metal surface. Such optimization of the intermolecular landscape at both bulk and interface levels effectively enhances cycling stability and capacity retention. Specifically, the approach enabled NMC811‖Li full cells to cycle for over 500 cycles at 4.3 V, with greater than 90% capacity retention.[78] These findings underscore how precise molecular engineering—whether focused on the polymer or the salt—can critically tune the multifaceted intermolecular interactions within polymer electrolytes, driving superior electrochemical performance and durability in next-generation high-energy LMBs.

Another central concept in optimizing these electrolytes involves network structuring within the polymer matrix to achieve an optimal compromise between mechanical robustness and efficient ion transport. For example, in entanglement–association polymer electrolytes consisting of poly(vinylidene fluoride-*co*-hexafluoropropylene) (PVFH) with a copolymer stabilizer (PVCA), it was found that weak, reversible dynamic associations foster an entangled network that simultaneously allows the promotion of continuous Li^+ conduction pathways while offering elasticity sufficient to withstand and suppress lithium dendrite growth in metallic lithium batteries. This dual regulation produces membranes with superior room-temperature ionic conductivity and supports long-term electrochemical cycling even at high current densities, preserving substantial capacity after hundreds of cycles. Beyond simple matrices, innovative structural engineering has led to the design of microdomain-engineered solid polymer electrolytes (SPEs) in which well-defined interfaces and internal spatial patterning facilitate high conductivities by supporting directional pathways and reducing tortuosity, while new rigid-rod polymer architectures enable anisotropic ion transport, channeling ion flux with minimal scattering by orienting conductive segments along preferred directions.[79] Wang *et al.* reported entanglement–association polymer electrolytes based on a PVFH–PVCA matrix, in which weak yet dynamic associ-

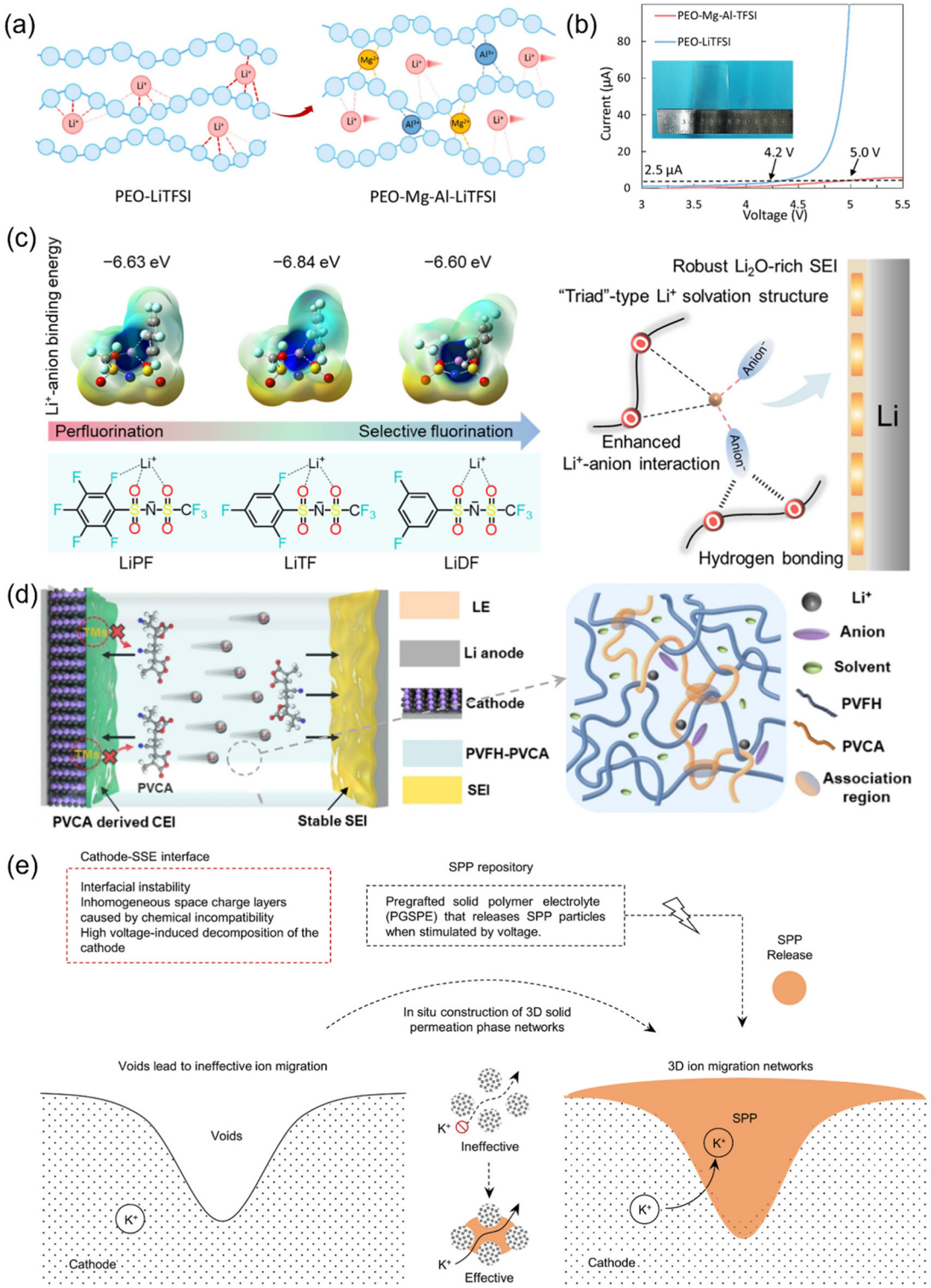

Fig. 6 (a) Schematic of the function of Lewis-acid additives.[28] (b) Linear sweep voltammetry curve of PEO–LiTFSI and PEO–Mg–Al–LiTFSI electrolytes, with the threshold current of 2.5 μA.[28] (c) The fluorination strategy and binding energy values of selectively fluorinated aromatic lithium salts.[78] (d) schematic illustration of the stable solid electrolyte interphase (SEI) formed on the Li-metal anode and the inhibited degradation of the cathode interface layer in a Li-metal cell using the PVFH–PVCA polymer electrolyte.[79] (e) A permeable 3D SSE with excellent bonding with the cathode is constructed by creating a solid permeation phase (SPP) *in situ* from a PGSPE to fill the voids for a void-free interfacial contact.[80]

ations fostered a highly entangled network. This architecture enables fast Li^+ conduction and ensures membrane elasticity that effectively resists dendrite growth (Fig. 6d). As a result, these membranes deliver remarkable room-temperature ionic conductivities (close to 10^{-4} S cm^{-1}), are able to cycle Li‖Li systems stably for more than 4500 hours at 8 mA cm^{-2}, and retain 84.7% capacity after 400 cycles in full cells at 4.8 V.[79] Expanding the design paradigm, Li *et al.* engineered microdomain-based solid polymer electrolytes (SPEs), which possess well-defined interfaces and internal phase separation, where ion channels are structured at the micro-scale to facilitate directional lithium transport and enhance conductivity—a direct result of tuning polymer microstructure to optimize ion pathways.[82] Complementarily, Gou *et al.* devised rigid-rod polymer systems exhibiting increased anisotropy in ion movement and conductivity by promoting alignment along preferred directions within the polymer matrix.[83]

Interfacial stability is also critically governed by intermolecular interactions. In this regard, the development of stimulus-responsive pregrafted solid polymer electrolytes (PGSPEs), composed of PVPI and PEO, is of great significance. The PGSPE framework undergoes a voltage-induced phase transition, generating a solid permeation phase replete with ion channels (Fig. 6e). This structural adaptability ensures the formation of void-free, ion-conductive interfaces at the electrode, supporting over 1000 hours of Li‖Li cell cycling and promoting high rate capability in full cells.[80] The regulatory effect of intermolecular design additionally includes innovative composite systems. For instance, the introduction of Zn-MOF into the polymer architecture leads to an improvement in both ionic transport and interfacial stability, resulting in exceptionally stable and continuous lithium cycling under testing conditions.[84]

Perhaps most transformative in ion selectivity are single-ion conducting polymer electrolytes (SICPEs). In these advanced systems, the anion moiety is chemically bonded to the polymer matrix, resulting in ultra-high lithium transference (*e.g.*, 0.85 for PEG-based SICPE) and substantial dendrite suppression, as both demonstrated *via* over 80 days of dendrite-free operation in Li‖Li cells and strong capacity retention at multiple rates in $LiFePO_4$‖Li full cells.[85]

Taking polymer electrolyte technology towards manufacturing scale, Lee *et al.* presented a methodology for robust parameterization in pouch cell production. Here, the optimization of mixing, calendaring, lamination, and stack pressure—directly modulated by intermolecular forces and dynamic interfaces—enables stabilization of Li metal cycling at multi-Ah scales.[86] In parallel, Newman *et al.* introduced an adaptive polymer interlayer that dynamically adjusts in response to operational stress in LMBs, further verifying the crucial influence of polymer–polymer interaction and adaptability in practical architectures.[87]

Among polymer-based electrolyte strategies, organic–inorganic composite electrolytes deserve particular attention because they offer a realistic route to reconcile several competing requirements in high-energy-density LMBs. In these systems, the polymer phase provides conformal interfacial contact, flexibility, and processability, whereas the inorganic phase can contribute mechanical reinforcement, improved oxidative stability, and, in some cases, fast Li^+-transport pathways. Their practical significance therefore lies not merely in combining the properties of two components, but in partially bridging the long-standing trade-off between soft-contact interfaces and robust solid-state stability. Compared with purely polymeric electrolytes, composite architectures can better suppress local deformation and improve high-voltage tolerance; compared with purely inorganic electrolytes, they often offer superior electrode wetting, lower contact resistance, and more accessible processing routes. As such, composite electrolytes can be regarded as an important transitional platform toward practical high-energy-density LMBs.

Recent representative studies further show that composite concepts can be implemented through several distinct but related routes. One important route relies on inorganic-filler-reinforced or phase-regulated polymer matrices, where the inorganic component is not merely a passive mechanical additive but also actively regulates local coordination environments and microstructural continuity. In this regard, Wu *et al.* demonstrated that phase regulation can be used to construct dense polymer-based composite electrolytes, highlighting how dense composite organization and optimized phase distribution are crucial for simultaneously improving ionic transport and solid-state robustness.[88]

A second route involves structurally engineered hybrid architectures that use functional separation to balance interfacial conformity with structural robustness. For example, the PGSPE-based permeable 3D SSE reported in this review forms a solid permeation phase (SPP) *in situ*, which fills cathode-side voids and enables void-free interfacial contact, thereby illustrating how permeable composite architectures can directly address one of the most persistent bottlenecks of solid-state cells—poor electrode–electrolyte integration.[80] Likewise, the Zn^{2+}-bridged polyether electrolyte shows that hybrid interaction engineering within a quasi-solid matrix can simultaneously improve oxidative stability, mechanical resilience, and practical pouch-cell output, emphasizing that composite concepts are not limited to filler addition but can also emerge from ion-bridged hybrid network design.[81]

A third route focuses on framework-mediated or integrated architectures. The Zn-MOF-regulated polymer system further illustrates how hybrid fillers can reshape polymer architectures and improve both ionic transport and interfacial stability.[84] Beyond this, Fan *et al.* proposed a fiber-network-based composite solid electrolyte strategy, Guo *et al.* reported COF-mediated foldable solid-state batteries, and Hu *et al.* developed an *in situ* polymerized integrated ultrathin solid electrolyte/cathode design; taken together, these studies show that composite concepts can also be realized through framework guidance, scaffold-assisted organization, or direct cathode–electrolyte integration rather than through conventional particle-filled matrices alone.[89–91]

Importantly, from a manufacturing and scale-up perspective, the production-oriented parametrization reported by Lee

et al. also suggests that hybrid polymer-electrolyte concepts are highly relevant not only for laboratory-level performance optimization but also for practical pouch-cell fabrication.[86] Collectively, these examples indicate that the value of composite electrolytes lies not simply in property averaging, but in enabling multidimensional optimization of contact, transport, robustness, and processability.

Nevertheless, their performance still critically depends on the compatibility between polymer and inorganic phases, the continuity of Li^+-transport pathways, and the control of interfacial resistance across multicomponent domains.

For polymer and quasi-solid electrolytes, the key challenge is likewise dual-sided rather than exclusively anode-centred. In addition to suppressing dendrite growth and accommodating Li-metal volume change, these electrolytes must also withstand oxidative conditions at high-voltage layered-oxide cathodes and maintain chemically and mechanically stable cathode-side interphases. From this perspective, strategies such as Lewis-acid coordination, ion-bridged network construction, and fluorinated/anion-engineered polymer electrolytes are valuable not only because they improve Li^+ transport and anode interfacial stability, but also because they broaden the oxidative stability window and enhance cathode compatibility. Therefore, future polymer-electrolyte design should place equal emphasis on Li-metal protection and cathode-side oxidative stability under practical high-voltage conditions.

More generally, wetting/contact evolution is a critical but often underemphasized variable in polymer, gel, and quasi-solid electrolytes. Good wetting and conformal interfacial contact help homogenize Li^+ flux, lower local polarization, and promote uniform interphase formation at both electrodes. By contrast, insufficient wetting or contact loss can generate local current hotspots, interfacial voids, and spatially heterogeneous reaction environments, which accelerate parasitic decomposition, non-uniform Li deposition, and mechanical degradation. This issue can be particularly severe for solid-state contact with polycrystalline high-voltage cathodes, where incomplete electrolyte infiltration may leave inner primary particles insufficiently passivated, aggravate oxygen release, and intensify interfacial exothermic reactions.[92] In this sense, wetting is not only an electrochemical issue related to rate capability and cycle life, but also a safety-relevant factor because local interfacial inhomogeneity can amplify heat generation and failure risk under high-voltage, lean-electrolyte, or wide-temperature conditions. More broadly, recent safety analyses of solid-state batteries have likewise emphasized that solid-phase interfaces are central determinants of thermal-runaway-related behaviour.[93] Therefore, future electrolyte design should treat wetting/contact management as an integral part of interfacial engineering rather than a secondary consequence of bulk electrolyte selection.

3.2 Polymer solvation structures

The solvation structure of polymer electrolytes is a fundamental aspect governing their ionic conductivity, electrochemical stability, and ultimately their effectiveness in LMBs aiming for energy densities as high as 500 Wh kg^{-1}. In contrast to liquid electrolytes, where solvent molecules freely surround and solvate Li^+ ions, in solid polymer electrolytes (SPEs), the polymer matrix itself acts as both the "solvent" and framework for ionic migration. This results in unique solvation behaviors and transport mechanisms tailored by the local coordination environment of the lithium ions within the polymer host.

In archetypal SPEs such as those based on polyethylene oxide (PEO), lithium ions are coordinated by the ether oxygens of the polymer chains, forming transient solvation structures as the polymer segments move. The mobility of these chains, driven by thermal fluctuations, is tightly coupled to the ionic conductivity: more flexible matrices with higher segmental motion typically afford greater ion transport. However, this also results in a delicate trade-off—enhancing segmental mobility for higher conductivity may compromise mechanical stability and the ability to suppress dendrite formation when paired with lithium metal anodes.

The concentration and nature of lithium salts, as well as the architecture of the polymer itself, further modulate the solvation structure. High salt concentration can induce ion aggregation or clusters, reducing the population of "free" Li^+ ions contributing to conductivity, while low concentrations can limit the number of conduction charge carriers. The choice of the anion is also critical: bulky, weakly coordinating anions can promote more dissociated—and thus conductive—solvation structures, whereas strongly coordinating anions may form ion pairs or complexes that hinder lithium mobility.

To address the limitations of conventional polymer electrolytes, advanced designs increasingly focus on tailoring the solvation structure at the molecular level. Incorporation of polar functional groups, use of copolymer or block architectures, and blending with additives or nanoparticles can create more favorable Li^+ coordination environments. These modifications aim to optimize both mechanical integrity and solvation dynamics, allowing polymer electrolytes to achieve both high ionic conductivity and robust electrochemical stability—key requirements for high-energy-density LMBs.

Furthermore, the solvation structure strongly influences the formation and stability of the solid electrolyte interphase (SEI) at the lithium-metal surface. A well-designed solvation environment can promote the formation of a stable, ionically conductive SEI, enhancing cycle life and safety. The future direction of SPE design thus lies in fine-tuning polymer–ion and polymer–anion interactions to realize solvation structures that balance transport, stability, and interfacial compatibility in the pursuit of next-generation 500 Wh kg^{-1} LMBs.

Collectively, this body of work underscores the multifaceted significance of intermolecular interactions in advancing polymer electrolytes. From tailored entanglements and microdomain structuring to interfacial engineering and composite optimization, as well as single-ion-yielding manipulation, the coherent development of polymer–polymer and polymer–ion networks holds fundamental importance for improving ionic conductivity, outlining durability, inhibiting dendrites, and enabling technological scalability in future energy storage systems.

Although the main scope of this review focuses on lithium-metal batteries with conventional metallic lithium anodes, we also selectively highlight anode-free systems where the electrolyte design is directly transferable and the cathode belongs to the targeted family of layered oxide materials. A representative case of solvation structure engineering is presented by Huang *et al.* in a recent study, where a quasi-solid fluoropolyether-based polymer electrolyte (FPE-SPE) was developed to enhance high-voltage lithium-rich manganese oxide (LRMO) cathode compatibility.[94] By copolymerizing strongly solvating polyether segments with weakly solvating fluorohydrocarbon pendants, the authors constructed an anion-rich solvation shell that favors contact ion pair (CIP) and aggregate (AGG) formation. Central to this design is the formation of $F\cdots Li^+\cdots O–CH_2–$ type intersegmental coordination bridges, in which Li^+ is simultaneously coordinated by fluorinated side chains and polyether segments. This solvation structure reduces the Li^+ binding energy and shifts the coordination environment from free anions to compact ion clusters, thereby enhancing Li^+ transport while facilitating the formation of fluorine-rich CEI/SEI layers. In particular, a LiF-rich outer layer and Mn–F bonding within the inner CEI stabilize the LRMO surface, suppress lattice oxygen escape, and improve oxygen redox reversibility (Fig. 7a). These effects collectively enable the construction of anode-free pouch cells delivering an impressive energy density of 604 Wh kg^{-1}, based on the total cell mass. This work vividly illustrates how molecular-level solvation control can concurrently regulate ionic mobility and interfacial chemistry in solid polymer electrolytes.

Equally vital to the electrochemical and mechanical performance of polymer electrolytes is their solvation architecture, where the nature and distribution of coordinating solvent or liquid-phase moieties within the composite framework decide both the overall conductivity and long-term stability. A prime strategy in the recent literature is the regulated confinement of solvent mobility within solid-state frameworks. Zhu *et al.* achieved this balance by covalently tethering DMF molecules to PVDF–HFP polymer chains (Fig. 7b), thus generating an electrolyte with both liquid-like ionic conductivity ($\sigma \approx 6.5 \times 10^{-4}$ S cm^{-1}) and thoroughly resilient, solid-like cycling characteristics. This synergy delivered 6000 hours of Li||Li cycling at 0.1 mA cm^{-2} and over 1000 stable full-cell cycles at 1 C,[95] demonstrating the effectiveness of solvent—polymer integration.

Moving into gel-based systems, ionogels have gained recognition for their efficient solvation behavior. By incorporating ionic liquids as the solvent phase within a supramolecular ionogels (SIGs), Jiang *et al.* recently developed a SIG based on a low-molecular-weight gelator, 12-hydroxyoctadecanoic acid (12-HOA) (Fig. 7c), which can effectively immobilize the solvate ionic liquid [Li(G4)][TFSI] (SIL) using only 2 wt% of the gelator (Fig. 7d). The resulting quasi-solid-state electrolyte exhibits a high ionic conductivity of 1.091×10^{-3} S cm^{-1} at 25 °C, increasing to 4.623×10^{-3} S cm^{-1} at 95 °C, comparable to that of neat SIL. Remarkably, the ionogel demonstrates a thermally reversible gel-to-sol transition, enabling post-assembly electrolyte infiltration into porous electrode structures and subsequent solidification, which significantly improves electrode–electrolyte interfacial contact and reduces resistance, along with stable operation over 1000 hours of symmetric cell cycling and robust capacity retention during NMC811||Li cycles for over 200 iterations.[29]

Recent developments in the field of polymer electrolytes for lithium batteries have also highlighted the crucial importance of solvation structure control, particularly as the demand for batteries capable of operating reliably under extreme temperature conditions continues to rise. Chen *et al.* reported a gel polymer electrolyte (GPE) formulated from $LiBF_4$, 1,3-dioxolane (DOL), and fluoroethylene carbonate (FEC), where *in situ* polymerization of DOL yields a poly-DOL (PDOL) framework that directly participates in Li^+ solvation (Fig. 7e). This polymer-coordinated solvation structure effectively replaces BF_4^-, reducing Li^+ desolvation energy and enabling faster ion transport at low temperatures. The resulting SEI is enriched in LiF and $Li_xBO_yF_z$, contributing to interfacial stability and dendrite suppression. The GPE delivers 0.53 mS cm^{-1} conductivity at −20 °C (Fig. 7f), supports over 5500 hours of symmetric cycling, and enables full-cell operation down to −60 °C.[96]

Beyond conventional strategies that focus on modulating polymer segment mobility or introducing polar functional groups, Liu *et al.* introduced a novel bioinspired approach for tuning Li^+ solvation through polymer–solvent dipole coupling. They designed a weakly-solvated gel polymer electrolyte (WSGPE) by *in situ* polymerizing trifluoroethyl methacrylate (TFMA) into a brush-like PTFMA framework, alongside ethyl 3,3,3-trifluoropropanoate (FEP) as a dipole-altering additive. The strong dipole–dipole interactions between PTFMA side chains and FEP molecules effectively exclude FEP from the Li^+ solvation shell, giving rise to an anion-dominant, weak solvation environment that lowers Li^+ desolvation barriers and facilitates interfacial transport (Fig. 7g). The resulting electrolyte maintains a conductivity of 1.03×10^{-4} S cm^{-1} at −40 °C and supports stable Li||NCM811 cycling across a wide range from −30 °C to 80 °C. At −30 °C, the full cell delivers 121.4 mAh g^{-1}, which increases to 172.2 mAh g^{-1} at 80 °C, with 94% capacity retention after 100 cycles. The assembled pouch cells achieve an energy density of 490.8 Wh kg^{-1}. Interface analyses confirm SEI/CEI layers rich in LiF and Li_2O, arising from coordinated decomposition of BF_4^- and residual solvent at the interface (Fig. 7h), forming robust, ion-conductive inorganic-rich structures that suppress dendrites and parasitic reactions, enabling safe and efficient LMBs under extreme temperature conditions.[97]

A particularly promising frontier in polymer electrolyte design is the development of temperature-responsive materials. Gu *et al.* proposed a thermoresponsive ether-based electrolyte: by introducing 1,3,5-trioxane (TO) into a tetrahydrofuran (THF) system with a conventional salt concentration (1 mol L^{-1} lithium bis(fluorosulfonyl)imide, LiFSI), the authors achieved wide-temperature stability through temperature-dependent solvation regulation and *in situ* polymerization. At low temperatures (≤−40 °C), TO participates in the

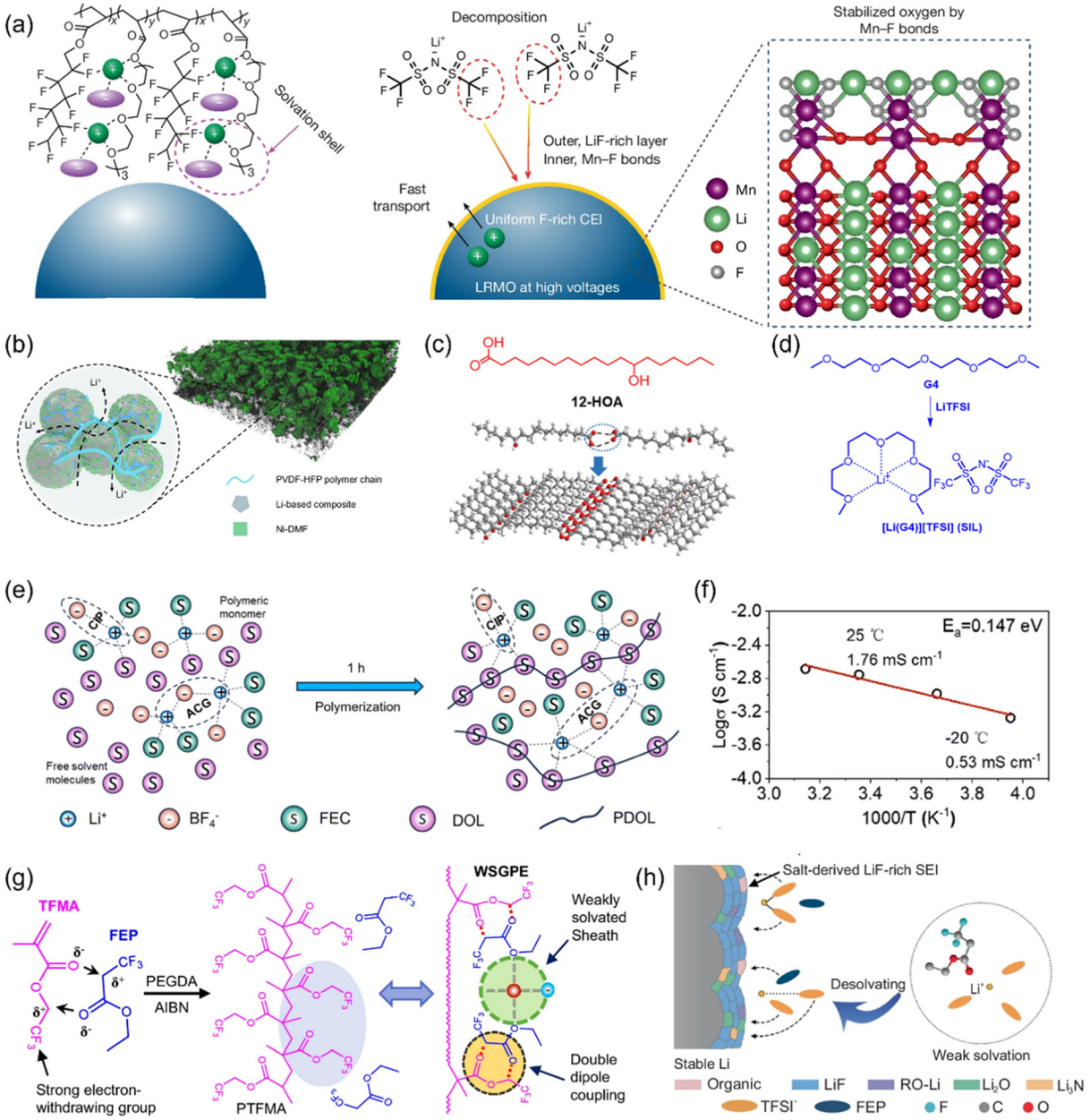

Fig. 7 (a) Stabilized LRMO surface oxygen by anion-derived CEI in fluoropolyether-based polymer electrolyte. Stage I is the *in situ* fluoropolyether-based electrolyte with anion-rich solvation; stage II is anion decomposition at the charging process; and stage III is Mn–F bonds suppressing O_2 escape.[94] (b) Schematic illustration of the internal architecture LPE@Ni-DMF (Ni-DMF incorporated into a LiFSI/poly(vinylidene fluoride-*co*-hexafluoropropylene) (PVDF-HFP) electrolyte (donated as LPE) to yield a CPE (donated as LPE@Ni-DMF)). The rendered green region represents the uniformly dispersed Ni-DMF nanosheets.[95] (c) 12-hydroxyoctadecanoic acid (12-HOA) could serve as an efficient low-molecular-weight gelator for the direct confinement of IL electrolytes; the possible aggregation model of 12-HOA molecules for gelation.[29] (d) Solvate ionic liquids (SIL) ([Li(G4)][TFSI], noted as "SIL") comprising an equimolar mixture of tetraglyme (G4) and lithium bis(trifluoromethane)sulfonimide (LiTFSI) were employed as the IL electrolytes.[29] (e) Scheme of interactions between components before and after polymerization.[96] (f) Ionic conductivities as a function of temperature for the GPE.[96] (g) Structures and fabrication method of WSGPE.[97] (h) Schematic illustration of Li-electrolyte interface of Li|WSGPE|Li batteries.[97]

Li^+ solvation sheath, weakening Li^+–THF coordination and enhancing Li^+–FSI^- coordination, leading to a contact ion pair (CIP)-dominated structure that accelerates Li^+ desolvation and improves charge-transfer kinetics. Simultaneously, a compact dual-layer SEI/CEI forms, consisting of a Li-polyoxymethylene (LiPOM) outer layer and LiF/Li_2O-rich inner layer, which suppresses THF/salt decomposition and dendrite growth. At elevated temperature (60 °C), TO triggers cationic ring-opening polymerization of THF to form a poly(tetrahydrofuran) (PTHF) network, scavenging free solvent and shifting the solvation

structure toward anion-aggregate-dominated AGG I/AGG II states. This transformation broadens the oxidative stability window (4.73 V) and enhances thermal safety. The strategy enables wide-temperature cycling stability: 87.3% capacity retention over 500 cycles at 25 °C, 90% over 200 cycles at −40 °C, and 88.9% over 400 cycles at 60 °C. A practical 1.5 Ah Li||NCM811 pouch cell achieves 317.1 Wh kg^{-1} at −40 °C and operates reversibly across −60 to 60 °C, demonstrating the feasibility of combining low-temperature kinetics with high-temperature safety under conventional salt concentrations and low viscosity.[98]

Sophisticated solvation manipulation also extends to high-concentration, single-phase polymer-in-salt formulations. In the study by Zhang *et al.*, the combination of a polymer-in-salt electrolyte with PVDF-HFP as a dilutor avoids traditional phase separation and instead allows for uniform LiF-rich interphase formation. This configuration not only secured strong conductivity ($\sigma \approx 3 \times 10^{-4}$ S cm^{-1}), but also facilitated a critical current density (CCD) of 3.7 mA cm^{-2} and ensured over 450 cycles in NMC811||Li cells at 4.5 V.[99] Here, the solvation strategy goes beyond simply maximizing the number of free ions or mobile solvent but focuses instead on achieving a uniform, stable ionic architecture at the electrode interface, which is crucial in preventing unwanted side reactions and electrode passivation.

The manipulation of the spatial arrangement of solvated ions within the polymer matrix has also come to the fore in the context of multi-structural and temperature-optimized polymer electrolytes. For instance, the refined multi-structural polymer electrolyte (RMSPE) demonstrates clear benefits: through precisely engineered domains and segmental arrangements, these systems achieve a conductivity of 0.93 mS cm^{-1} at −35 °C and an exceptionally wide oxidative stability window, reaching 5.1 V.[100] Such properties are exceedingly rare and underscore the efficacy of orchestrating solvation structures to shield electrochemical reactions from destructive by-products. Complementarily, Wang *et al.* have developed SPEs that maintain reliable lithium cycling even at −35 °C—a feat made possible by exact control over frozen solvation states and the microenvironment surrounding mobile ions.[101] These SPEs, through the fine tuning of polymer architecture and solvation chemistry, resist freeze-induced brittleness and conductivity loss, retaining both ion and charge mobility required for demanding, real-world battery applications.

In summary, these innovations demonstrate that the intelligent control of solvation structure, informed by both chemistry and molecular architecture, is paramount for the next generation of safe, flexible, and durable polymer electrolytes. Whether through bio-inspired gels, temperature-adaptive polymers, high-concentration phases, or spatially orchestrated multi-structural designs, it is clear that future batteries will rest on mastery of the dynamic landscape of solvation design.

Despite the impressive progress summarized above, the quoted energy-density values are often obtained under substantially different testing conditions, including cathode loading, Li excess, electrolyte dosage, cutoff voltage, and cell format. Therefore, direct comparison based solely on reported Wh kg^{-1} values may be misleading. To facilitate a more application-relevant benchmarking, representative practical demonstrations discussed in sections 2 and 3 are summarized in Table 1 using a simplified set of practical metrics, including cathode/loading information, Li-anode condition, electrolyte amount, cell format, energy density, and cycling performance.

As shown in Table 1, substantial progress has been achieved in liquid and polymer/quasi-solid electrolyte systems under increasingly practical conditions. By contrast, many inorganic solid-state electrolyte studies are still more frequently evaluated in terms of ionic conductivity, densification, air stability, and interfacial resistance, while sufficiently unified practical full-cell metrics are reported less consistently. This gap further motivates the discussion in section 4, which focuses on the remaining materials and interfacial challenges of inorganic SSEs toward practical deployment.

4. Inorganic solid-state electrolytes

Compared to traditional liquid electrolytes or polymer electrolytes, which may pose safety risks, the adoption of inorganic solid-state electrolytes (SSEs) in high-energy-density LMB systems is crucial for mitigating such hazards. Inorganic SSEs hold significant research importance in the development of LMBs. However, several key challenges remain for inorganic SSEs, including high interfacial charge-transfer resistance and poor mechanical flexibility. Inorganic SSEs are primarily categorized into oxides and sulfides. Oxide-based electrolytes exhibit superior environmental stability, with low sensitivity to moisture/oxygen, yet their relatively low ionic conductivity and poor interfacial contact hinder their application in high-energy-density LMBs. Sulfide-based electrolytes possess high ionic conductivity, but their extreme sensitivity to moisture and the interface stability issues impose limitations on their practical use. This section will focus on the optimization strategies for these two types of inorganic SSEs.

Although this section focuses on materials- and process-level bottlenecks—raising ionic conductivity in oxide SSEs and improving air/interfacial stability in sulfide SSEs—rather than reporting pouch-cell energy densities directly, these "first-principles" advances are prerequisite to any ≥500 Wh kg^{-1} architecture. For oxides, high mechanical modulus and wide-voltage stability translate into system-level energy gains only when room-temperature bulk and interfacial conductivities reach $\geq 10^{-3}$ S cm^{-1} and interfacial resistance is minimized, enabling thinner electrolytes, lower inactive mass, and compatibility with thin-Li and low E/C. For sulfides, liquid-like conductivity is not sufficient unless air sensitivity and electrode-side instability are mitigated to support high voltage, high loading, and long life in truly all-solid formats. By surveying lattice/doping/densification (sintering-aid) strategies for oxides and doping plus surface coating/reconstruction for sulfides, this section complements the preceding liquid-electrolyte routes and underscores two additional levers for future high-energy LMBs: more robust high-voltage windows and intrinsic

Table 1 Benchmark comparison of representative high-energy-density lithium metal batteries under practical metrics

Ref.	Electrolyte strategy	Representative system	Cathode/loading	Li anode	Electrolyte amount	Cell format	Energy density	Cycling performance
24	Liquid electrolyte; compressed solvation structure	Cl 7 electrolyte (ClDEE-based)	NCM811/30 mg cm^{-2}	100 μm Li, Cu-free	1.1 g Ah^{-1}	5.6 Ah pouch	510.3 Wh kg^{-1}	84% capacity retention after 116 cycles
34	Liquid electrolyte; trifluoromethylated ether/anion-dominated solvation	TMEE-2M (2 M LiFSI in TMEE)	NCM811/6 mAh cm^{-2}	30 μm Li	1.33 g Ah^{-1}	14 Ah pouch	512 Wh kg^{-1}	90% retention after 100 cycles
47	Liquid electrolyte; phosphate-based low-concentration electrolyte	TMP-0.7 M LiDFOB	NCM9055/28.9 mg cm^{-2} (5.8 mAh cm^{-2})	40 μm Li	1.8 g Ah^{-1}	20.0 Ah pouch	533.8 Wh kg^{-1}	>14 cycles demonstrated
48	Liquid electrolyte; wide-temperature electrolyte	WTAE (1 M LiFSI + 0.02 M $LiNO_3$ in DME : TTE = 3 : 7)	High-Ni cathode/NR	NR	NR	5.8 Ah pouch	503.3 Wh kg^{-1}	260 stable cycles at 25 °C
52	Liquid electrolyte; dielectric-mediated oscillatory solvation	PFB electrolyte	NCM811/26 mg cm^{-2}	100 μm Li	1.0 g Ah^{-1}	6 Ah pouch	500 Wh kg^{-1}	92% retention after 150 cycles
53	Liquid electrolyte; fluorinated hybrid diluent modulation	LHCE-TB (BTFE/TTE hybrid diluent)	NCM9055/≈25 mg cm^{-2}	50 μm Li	1.4 g Ah^{-1}	5.81 Ah pouch	508.5 Wh kg^{-1}	80.9% retention after 100 cycles
54	Liquid electrolyte; functional-divided hybrid diluent engineering	C-DHCE	NCM811/ 4.82 mAh cm^{-2}	25 μm Li	1.7 g Ah^{-1}	2.95 Ah pouch	518 Wh kg^{-1}	>92% retention after 107 cycles
55	Liquid electrolyte; compact ion-pair aggregate electrolyte	CIPA electrolyte (2 M LiFSI in EGBE/TTE, 1 : 1 v/v)	High-Ni cathode/ ~4.2 mAh cm^{-2}	60 μm Li	1.25 g Ah^{-1}	19 Ah pouch	505.9 Wh kg^{-1}	91% energy retention after 130 cycles
56	Liquid electrolyte; delocalized electrolyte	UDE	Ni90/NR	NR	1.0 g Ah^{-1}	5.5 Ah pouch	604.2 Wh kg^{-1}	>100 cycles demonstrated
57	Liquid electrolyte; monofluorinated hydrofluorocarbon electrolyte with weak F–Li^+ coordination and high wettability	1.13 M LiFSI/DFP	Ni96/33.5 mg cm^{-2} (7.32 mAh cm^{-2})	20 μm Li	0.56 g Ah^{-1}	13.33 Ah pouch	701.2 Wh kg^{-1}	91.6% retention after 30 cycles
60	Liquid electrolyte; additive-mediated anion-sieving coordination	MDFE (dual-salt electrolyte + MBTFA additive)	NCM811/≈31 mg cm^{-2}	50 μm Li	≈0.95 g Ah^{-1}	7.5 Ah pouch	≈541 Wh kg^{-1}	86% retention after 140 cycles
61	Interfacial functional material; salt-in-interlayer strategy	LNO–PVC interlayer	NCM811/NR	Li metal/NR	NR	Soft-pack pouch/NR	400 Wh kg^{-1}	Stable cycling over 65 cycles
62	Artificial interphase/molecular surface reconstruction	PFOA–Li reconstructed SEI	NCM90/≈39.6 mg cm^{-2}	100 μm Li	1.12 g Ah^{-1}	5.8 Ah pouch	518 Wh kg^{-1}	Stable cycling over 100 cycles
64	Interfacial functional material; micro-emulsion interfacial regulation	IM-F@AM-F micelle electrolyte	Ni90/NR	NR	1.0 g Ah^{-1}	7.2 Ah pouch	531 Wh kg^{-1}	81% retention after 189 cycles
65	Artificial interphase/sequential-reaction SEI	SPEI-derived multilayer SEI	NCM811/6.0 mAh cm^{-2}	Li metal/NR	1.35 g Ah^{-1}	3.4 Ah pouch	480.5 Wh kg^{-1}	85.9% retention after 100 cycles
81	Polymer/quasi-solid electrolyte; ion-bridged polyether electrolyte	Zn-IBPE	NMC90/4.86 mAh cm^{-2}	60 μm Li	NR	18 Ah pouch	452 Wh kg^{-1}	95.2% retention after 105 cycles
94	Polymer/quasi-solid electrolyte; in-built interfacial-layer polymer electrolyte	PTF-PE-SPE	LRMO/8 mAh cm^{-2}	Anode-free Cu (6 μm current collector)	1.2 g Ah^{-1}	9 Ah anode-free pouch	604 Wh kg^{-1}	Pouch voltage profiles explicitly shown to 15 cycles
97	Gel polymer electrolyte; weakly solvated gel polymer electrolyte	WSGPE	NCM811/23.4 mg cm^{-2}	50 μm Li	2.0 g Ah^{-1}	750 mAh pouch	490.8 Wh kg^{-1}	RT pouch cycling demonstrated

The values are summarized from the original reports and should be interpreted with caution, because cathode loading, Li excess, electrolyte dosage, cell format, and energy-density calculation boundaries are not fully standardized across the literature. NR indicates that the corresponding information was not explicitly reported in the accessible manuscript/SI.

dendrite suppression. Ultimately, these advances help connect materials mechanisms to device engineering and cell-level energy density, but their translation into practical oxide-based full cells still critically depends on resolving Li|electrolyte and cathode|electrolyte interfacial bottlenecks.

4.1 Oxide SSE elemental doping strategies

The ion transport mechanisms in SSEs differ significantly from those in liquid electrolytes. SSEs feature periodic bottleneck sites that form effective energy barriers, through which lithium ions must diffuse. The energy required to overcome these barriers (referred to as migration energy) profoundly influences ion mobility and conductivity. Lower migration energy leads to higher ion mobility and enhanced conductivity.

In oxide-based solid-state electrolytes, lithium-ion conductivity is influenced by the crystal structure, defect concentration, and the availability of diffusion pathways. In crystalline materials, ion transport primarily occurs *via* hopping between lattice sites, which depends on the presence of vacancies or under-occupied positions formed within the framework of coordination polyhedra (Fig. 8a). The most commonly observed lithium-ion diffusion mechanisms include the vacancy mechanism, interstitial mechanism, and the interstitial–substitutional exchange mechanism (Fig. 8b and c).[30] Specifically, vacancy transport relies on Schottky defects to provide hopping sites, while the interstitial mechanism involves lithium ions migrating through Frenkel defects *via* a knock-off process. Given that the type and distribution of defects determine the carrier concentration and diffusion be-

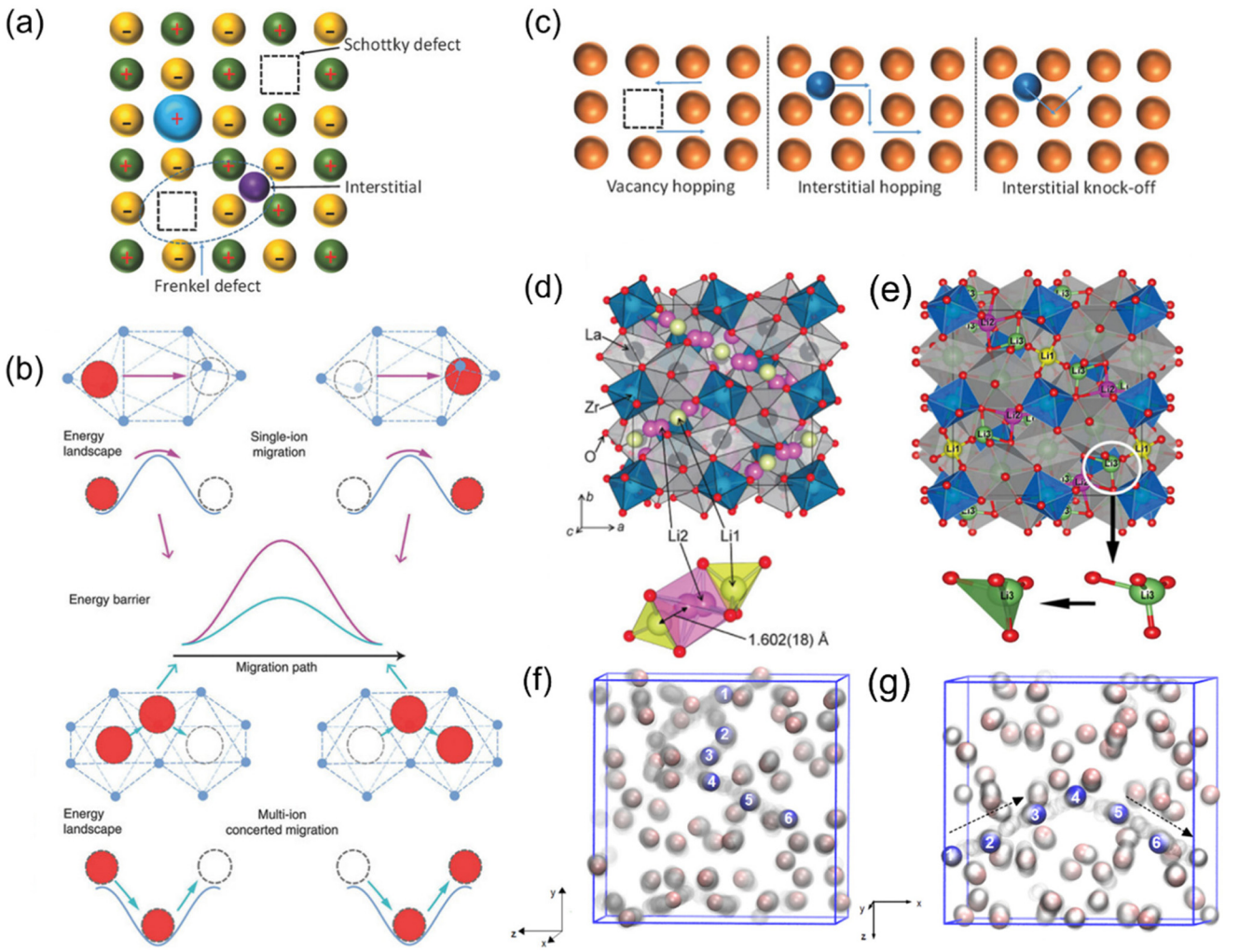

Fig. 8 Mechanism of ion transfer in inorganic solid electrolytes; (a) defect (b) migration pathway (c) migration mechanism in SSEs.[30] (d) Crystal structure of c-LLZO (coordination polyhedral around the Li1 and Li2 sites).[102] (e) Crystal structure of t-LLZO.[102] (f) Li-ion positions in the simulated unit cell of c-LLZO visualized for two different angles of view. (Transparent gray) Positions of Li ions (plotted every 0.15 ps) visited during 10 ps of metadynamics simulation at 300 K started from a cubic LLZO model structure. The more frequent a position is visited, the darker the color. (Solid) Li-ion positions of a geometry-optimized trajectory snapshot at 8.98 ps. Ions dominating characterization of the conduction pathway are indexed 1–6 and colored blue.[103] (g) Li-ion positions of t-LLZO as observed from metadynamics simulation at 300 K. Transparent gray: all Li-ion positions visited during 10 ps run. Solid: starting configuration of Li ions. Blue: ions involved in collective motion. Arrows indicate the direction of motion.[103]

havior, elemental doping has become a widely adopted approach for tailoring defect structures and improving lithium-ion mobility. In particular, aliovalent doping can introduce extra charge carriers or modify lattice geometry to widen lithium transport channels.[104] The following section systematically reviews how doping strategies have been applied to optimize the ionic conductivity of garnet-type, NASICON-type, and perovskite-type materials.

Ideally, the ionic radius of the dopant should be larger than that of the host element, thereby expanding the ion transport channel and promoting carrier migration.[105] For instance, the garnet-type oxide electrolyte $Li_7La_3Zr_2O_{12}$ (LLZO), which exhibits relatively high ionic conductivity among oxide-based SSEs, has emerged as a promising candidate for high-energy-density solid-state LMBs.

LLZO can crystallize in two primary phases: cubic (c-LLZO) and tetragonal (t-LLZO). Notably, c-LLZO exhibits one to three orders of magnitude higher ionic conductivity than its tetragonal counterpart. This significant difference arises from the disordered and partially occupied Li sites in the cubic phase, particularly at the 24 d (Li1) and 96 h (Li2) positions, which facilitate more percolative Li-ion transport pathways (Fig. 8d and e). In contrast, t-LLZO features fully ordered Li distribution at high-symmetry lattice sites, resulting in more constrained diffusion.[102] Furthermore, c-LLZO supports a lower-energy, asynchronous single-ion hopping mechanism, while t-LLZO relies on high-energy concerted motion, as confirmed by computational modeling (Fig. 8f and g).[103] By increasing the sintering temperature, the crystal structure of LLZO can be transformed from the tetragonal phase to the cubic phase.[30,106] The cubic-phase crystal structure of LLZO can be effectively stabilized through trace atomic doping. Furthermore, aliovalent substitution of Zr with Sb, Ta, or Nb enables modification of Li^+ arrangements in both octahedral and tetrahedral sites within the garnet-type oxide framework, thereby significantly enhancing the Li^+ conductivity of LLZO. In pioneering research on garnet-type oxides, Jin *et al.* demonstrated that minimal aluminum doping could stabilize the cubic structure of $Li_{6.25}La_3Zr_2Al_xO_{12}$, simultaneously elevating its room-temperature ionic conductivity to 0.2 mS cm^{-1}.[107] Murugan *et al.* successfully stabilized the cubic-phase lithium garnet structure by partially substituting Zr^{4+} with Te^{6+} in LLZO through optimized doping, achieving a room-temperature ionic conductivity of up to 1.02 mS cm^{-1}. Notably, this Te-doped $Li_{6.5}La_3Zr_{1.75}Te_{0.25}O_{12}$ compound could be initially synthesized at a relatively low sintering temperature (750 °C).[108] Llordés *et al.* developed a dual doping strategy (Ga^{3+} on Li sites and Sc^{3+} on Zr sites) to achieve Li^+ conductivity of 1.8 mS cm^{-1} in garnet-type LLZO through optimized Li-site occupancy and charge compensation; they demonstrated that this approach stabilizes the cubic phase while increasing Li^+ mobility.[109] Zhu *et al.* developed a unique terrace-shaped LLZO-Ga solid electrolyte with two-dimensional-like growth characteristics, exhibiting strong (420) preferred orientation and achieving an exceptional ionic conductivity of 2.06 mS cm^{-1} at room temperature.[110] Hwang *et al.* synthesized an air-stable, dual-doped (Ga, Nb)-LLZO cubic-phase garnet solid electrolyte ($Li_{6.05}La_3Ga_{0.3}Zr_{1.95}Nb_{0.05}O_{12}$) *via* a sol–gel process, achieving a to-date record-high ionic conductivity of 9.28 mS cm^{-1}.[111]

In another category of NASICON-type oxide solid electrolytes, $Li_{1+x}Al_xTi_{2-x}(PO_4)_3$ (LATP) is achieved by substituting partial Ti^{4+} in $LiTi_2(PO_4)_3$ (LTP) with smaller Al^{3+} ions, effectively reducing lattice dimensions and lowering the Li^+ migration energy barrier. Optimal Al^{3+} doping concentration is a critical factor in enhancing LATP's ionic conductivity. Studies utilizing nuclear magnetic resonance (NMR) and electrochemical impedance spectroscopy (EIS) characterization have revealed that grain boundary conductivity increases with Al^{3+} content, while bulk grain conductivity shows no significant improvement due to the upper limit of Al^{3+} doping in LATP. This limitation occurs because excessive Al^{3+} doping ($x > 0.5$) leads to the formation of secondary $AlPO_4$ phases, which subsequently impedes Li^+ diffusion kinetics.[112–114] Kanchan *et al.* elucidated the critical role played by dopant ionic radii on the material's structure and properties. They prepared $Li_{1.3}Al_{0.3-x}R_xTi_{1.7}(PO_4)_3$ (R = Ga^{3+}, Sc^{3+}, Y^{3+}) NASICON ceramics *via* solid-state reaction to investigate the effects of trivalent cation doping (x = 0.01–0.07) on Li^+ conductivity. Through X-ray diffraction, density measurements, and impedance spectroscopy, they found that although doping reduced material porosity, the overall Li^+ conductivity did not improve. Larger Sc^{3+} and Y^{3+} dopants tended to segregate at grain boundaries due to size mismatch, hindering Li^+ migration, while Ga^{3+} exhibited higher conductivity (~10^{-3} S cm^{-1}) by substituting both Al^{3+} and Ti^{4+} sites.[115] Liu *et al.* enhanced LATP's ionic conductivity by doping with larger-radius Te ions, partially substituting Ti with Te to prepare $Li_{1.3}Al_{0.3}Te_{0.03}Ti_{1.67}(PO_4)_3$. This Te substitution increased the lattice parameters of LATP and widened Li^+ transport channels, boosting bulk ionic conductivity from 1.67×10^{-4} S cm^{-1} to 7.03×10^{-3} S cm^{-1}.[116]

The perovskite-type solid-state electrolyte lithium lanthanum titanate $Li_{3x}La_{(2/3-x)}TiO_3$ (LLTO) has been regarded as a promising candidate for SSEs in solid-state batteries since its first report in 1993, due to its high ionic conductivity at room temperature, suitable electrochemical window, and excellent oxidation stability. In the 1993 report, the LLTO ($Li_{0.34}La_{0.51}TiO_{2.94}$) solid-state electrolyte exhibited bulk and total ionic conductivities of 1 mS cm^{-1} and 2×10^{-2} mS cm^{-1}, respectively.[117] Early studies explored enhancing the ionic conductivity of perovskite-type SSEs through elemental doping. In the perovskite crystal structure, lithium ions may encounter resistance due to oxygen ion blockage when moving from one site to another; significant efforts have been made to increase the perovskites' lattice constants, as this could potentially alter the magnitude of such resistance. For instance, Inaguma *et al.* improved the lattice parameters of the perovskite structure by doping Sr^{2+} into $Li_{0.5}La_{0.5}TiO_3$ to partially substitute La and Li, achieving a bulk ionic conductivity of 1.5 mS cm^{-1}.[118] The ideal perovskite-type material has a general chemical formula of ABO_3. The solid-state electrolyte $Li_{3x}La_{2/3-x}TiO_3$ (LLTO) is derived from A-site-deficient $La_{2/3}TiO_3$, where one La^{3+} ion can be replaced by three Li^+. Thus, the chemical formula of this

material can be expressed as $Li_{3x}La_{2/3-x}TiO_3$, with $(1/3 - 2x)$ A-site vacancies per formula unit. Elemental doping of LLTO aims to increase Li^+ concentration, enhance A-site vacancy density, and expand the size of Li^+ transport channels. Ozdemir *et al.* prepared $Li_{0.5}La_{0.5}Ti_{1-x}Al_xO_3$ (LLTAlO) materials with varying Al doping levels (x) *via* solid-state reaction. The results demonstrated that LLTAlO (x = 0.01, 0.05, 0.10) exhibited higher ionic conductivity than pure LLTO, confirming that trace Al doping effectively enhances the ionic conductivity of LLTO-based materials.[119] Son *et al.* synthesized Y-doped $Li_{0.33}La_{0.56-x}Y_xTiO_3$ (x = 0.02, 0.05, 0.1) *via* the sol–gel method, revealing that Y^{3+} (0.90 Å) with an intermediate ionic radius between Li^+ (0.76 Å) and La^{3+} (1.03 Å) reduces lattice distortion and promotes LLTO cubic phase formation, achieving optimal bulk conductivity (9.51×10^{-4} S cm^{-1} at 25 °C) for $Li_{0.33}La_{0.46}Y_{0.1}TiO_3$.[120] The Nd-doped LLTO (LLNT) demonstrated similar enhancement effects, where 0.5 mol% Nd doping increased the volume fraction of A-site disordered cubic phase, achieving record room-temperature Li^+ conductivity (1.26×10^{-3} S cm^{-1}), a 1.33-fold improvement compared to the undoped sample.[121] Some research studies have indicated that when larger-radius ions such as Sr^{2+} and Ba^{2+} are doped into La^{3+} sites in LLTO, the expansion of Li^+ transport channels leads to enhanced ionic conductivity.[122–124] Lu *et al.* prepared 0.25 mol% Sr^{2+}-doped LLTO materials *via* solid-state reaction, achieving an improved bulk conductivity of 1.17×10^{-3} S cm^{-1}.[122] Teranishi *et al.* demonstrated the optimizing effect of Ba^{2+} doping on LLTO conductivity and established a correlation mechanism between the cubic phase fraction and ionic conductivity.[123]

4.2 Sintering aids addition of oxide SSEs

Inorganic solid electrolytes are typically fabricated by sintering powders into pellets, where the Li^+ transport resistance at grain boundaries cannot be neglected. Optimizing Li^+ transport across grain boundaries is a critical challenge for effectively enhancing the ionic conductivity of oxide-based solid electrolytes, and increasing the densification of electrolyte particles helps reduce grain boundary impedance. Taking LATP as an example, researchers have conducted detailed studies on the influence of sintering temperature on the Li^+ conductivity of LATP oxides. The results indicate that the density, crystallinity, and ionic conductivity of LATP increase with higher sintering temperatures, while elevated temperatures also help eliminate impurity phases.[127] However, conventional sintering methods require high temperatures and prolonged durations to achieve sufficient densification of the material. Several emerging alternative sintering techniques have been proposed, such as spark plasma sintering (SPS), field-assisted sintering technology (FAST), and microwave sintering.[128–130] Nevertheless, the most widely used method to enhance the sinterability of ceramic materials remains the addition of low-melting-point sintering aids. During high-temperature sintering, the molten sintering aids promote uniform grain growth, improve intergranular contact, and enhance the sinterability of the material. The addition of sintering aids mainly involves two processes. The first is to use excess initial raw materials as sintering additives. The second is to mix oxide powder with additives to form dense particles before pressing and sintering (Fig. 9a).

Chen *et al.* proposed a low-temperature preparation method (<900 °C) for high-performance LATP using sintering aids (Li_3PO_4, $LiBO_2{\cdot}0.3H_2O$, and their binary composite). The results demonstrated that these sintering aids promote grain rearrangement and fill intergranular voids, significantly enhancing the density and ionic conductivity of LATP (up to 5.2×10^{-4} S cm^{-1}) while reducing activation energy. Compared to conventional high-temperature sintering (950 °C) of pure LATP without sintering aids, the conductivity was improved by 7.3 times (Fig. 9b and c).[31]

Luo *et al.* introduced $Li_2CO_3{\cdot}Bi_2O_3$ (LB) as a sintering aid, which remarkably improved both the sinterability and ionic conductivity of LATP solid electrolytes. The addition of LB enabled liquid-phase sintering at 900 °C, resulting in doubled grain size, increased relative density to 95.28%, and achieved a total ionic conductivity of 6.73×10^{-4} S cm^{-1}, over 4 times higher than that of LB-free samples sintered at the same temperature.[131] Furthermore, various inorganic compounds such as $Li_2B_4O_7$,[127] Li_2WO_4,[132] LiF,[133] and TeO_2 [134] have also been investigated as effective sintering aids to enhance the ionic conductivity of LATP while reducing its sintering temperature.

For garnet-type SSEs, the introduction of sintering aids primarily involves mixing LLZO powder with additives, followed by pressing and sintering to form dense pellets. Al_2O_3 as a sintering additive has been demonstrated to serve multiple functions. For instance, Zhao *et al.* revealed that the fundamental reason for the poor sinterability of LLZO is the presence of a Li_2CO_3 surface layer. The incorporation of Al_2O_3 during sintering promotes the decomposition of insulating Li_2CO_3 and generates the fast Li-ion conductor $LiAlO_2$, significantly improving the electrolyte's density, ionic conductivity, and wettability with lithium metal (Fig. 9d). The room-temperature ionic conductivity increased from 4.9×10^{-5} S cm^{-1} to 3.1×10^{-4} S cm^{-1}.[125] Meanwhile, Liu *et al.* employed atomic layer deposition (ALD) to construct a conformal nanoscale amorphous Al_2O_3 coating on LLZTO particles, reducing the sintering temperature of the garnet electrolyte to 980 °C (Fig. 9e). The resulting Li–Al–O grain-boundary phases exhibited ionic conduction while blocking electronic transport, achieving a high ionic conductivity of 0.13 mS cm^{-1}, a critical current density of 0.52 mA cm^{-2}, and cycling stability exceeding 5000 hours.[126] Another study reached similar conclusions, demonstrating that Al_2O_3 as a sintering additive reacts with Li_2CO_3 to form $LiAlO_2$ at grain boundaries; the resulting Li–Al–O secondary phases at grain boundaries effectively reduce electronic conductivity while maintaining Li^+ conductivity.[135] Certainly, some sintering additives are introduced as excess initial raw materials. For instance, Qin *et al.* incorporated an appropriate amount of La_2O_3 during the initial material preparation stage to regulate the distribution of Ta elements in $Li_{6.5}La_3Zr_{1.5}Ta_{0.5}O_{12}$ (LLZTO). This approach effectively eliminated Ta_2O_5 precipitates and engineered the grain boundary structure of LLZTO.

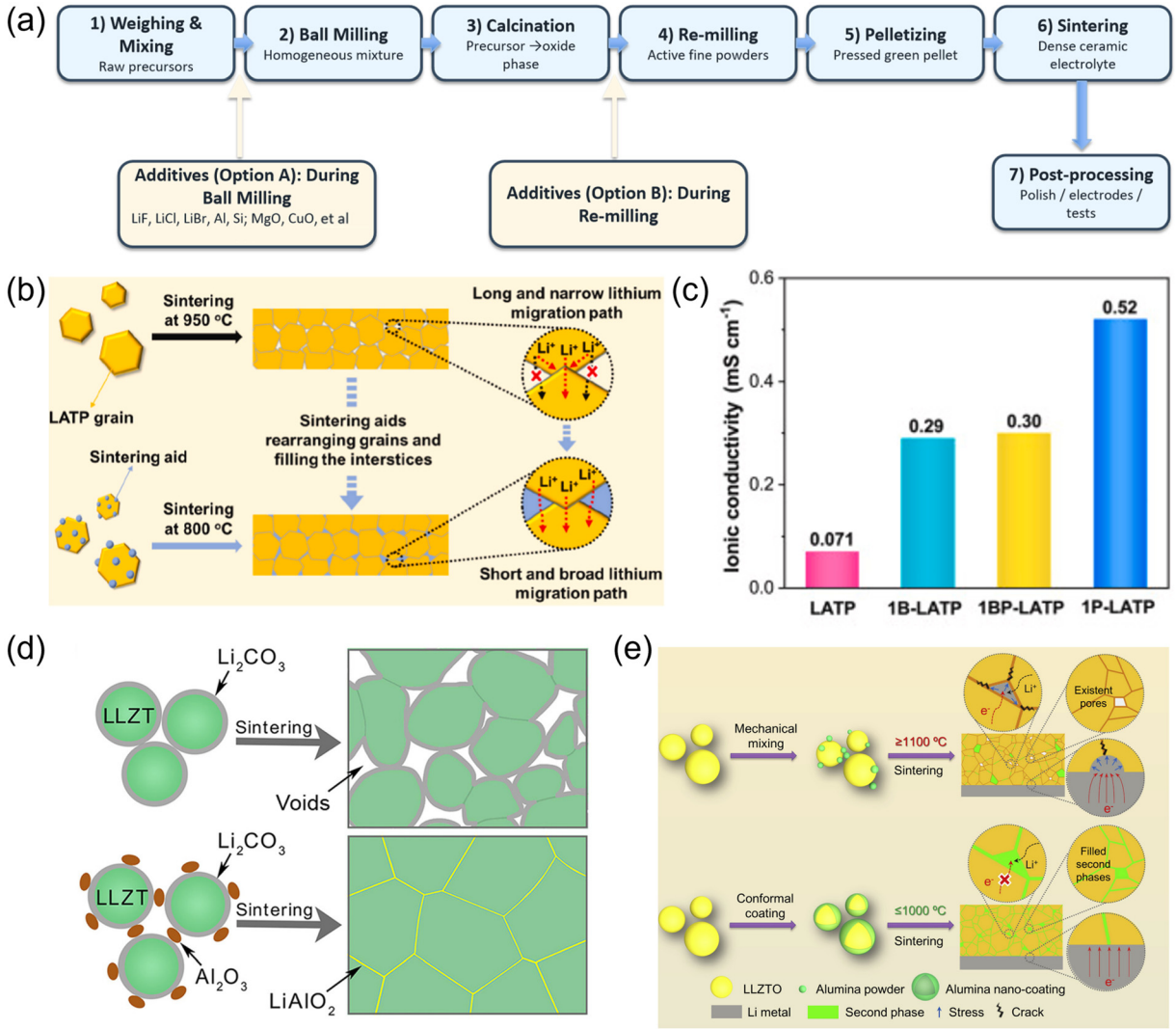

Fig. 9 (a) A scheme demonstrating the preparation process of sintering additive-assisted ceramic electrolytes. (b) Schematic illustration of lithium-ion migration paths between grains in pure LATP and 1P-LATP pellets.[31] (c) Ionic conductivities of LATP, 1B-LATP (sintering aids $LiBO_2{\cdot}0.3H_2O$), 1BP-LATP (sintering aids binary $0.32Li_3PO_4{-}0.68LiBO_2{\cdot}0.3H_2O$), and 1P-LATP (sintering aids Li_3PO_4) pellets at room temperature.[31] (d) Illustration of the function of Al_2O_3 additive in the sintering process of LLZTO.[125] (e) Different microstructures of the garnet-type solid electrolyte prepared by conventional pressureless sintering with sintering aid by traditional ball milling and conformal nanocoating.[126]

The sufficient reaction between La_2O_3 and Ta_2O_5 reduced the formation of void defects at grain boundaries, suppressed defects, and enhanced the relative density (reaching ~98%).[136,137] The effect of second phases such as amorphous SiO_2, $Li_2O{-}B_2O_3$, Li_3PO_4, and $LiO_2{-}SiO_2{-}B_2O_3$ in perovskite-type solid electrolytes has also been investigated and demonstrated to form space charge layers to solve the problem of high grain boundary resistance.[138–141]

Although elemental doping and sintering-aid engineering are primarily developed to improve bulk/grain-boundary transport in oxide SSEs, their benefits to interfacial compatibility should be understood as indirect rather than sufficient. In general, higher densification, reduced porosity, and more homogeneous grain-boundary networks can alleviate local current constriction, reduce contact loss, and improve mechanical uniformity at electrode|electrolyte interfaces. From this perspective, doping- and sintering-enabled microstructural optimization can help suppress local hotspots in Li^+ flux and partially mitigate the interfacial impedance growth associated with poorly consolidated oxide pellets. However, these improvements do not automatically resolve the fundamental challenges of oxide SSE interfaces, including poor wetting against Li metal, rigid solid–solid contact, chemo-mechanical mismatch during cycling, and persistent cathode-side contact/oxidation issues under high-voltage operation. Therefore, improvements in ionic conductivity and densification should be viewed as enabling prerequisites, but not direct substitutes, for dedicated interfacial engineering.

Importantly, convincing demonstrations under practically relevant conditions—such as high-loading cathodes, thin Li,

lean Li inventory, and low stack pressure—remain comparatively limited for many oxide SSE systems discussed here. As a result, translating improved pellet-level conductivity into high-energy full-cell performance still requires coordinated optimization of interfacial chemistry, mechanical compliance, electrode architecture, and processing compatibility.

4.3 Enhancement of air stability in sulfide SSEs

Sulfide SSEs have emerged as one of the most promising candidates for high-energy-density all-solid-state batteries. In contrast to oxide electrolytes, sulfides exhibit superior ionic conductivity. Since the breakthrough report of $Li_{10}GeP_2S_{12}$ (LGPS) in 2011, the ionic conductivity of sulfide SSEs has reached the order of 10^{-3}–10^{-2} S cm^{-1}, with some sulfide electrolytes even surpassing the conductivity of liquid electrolytes.[142–145] This demonstrates that ionic conductivity is no longer the limiting factor for energy density improvement in sulfide-based systems, while their air stability and electrochemical stability have become the critical bottlenecks hindering large-scale applications.

Currently, there are two primary approaches for enhancing the air stability of SSEs: elemental doping and protective surface coating. Elemental doping strategies are predominantly guided by the Hard and Soft Acids and Bases (HSAB) theory. For instance, a recent study based on HSAB theory successfully developed a novel sulfide electrolyte Li_6PS_5I-*x*Sn (LPSI-20Sn) by substituting the soft acid P^{5+} with Sn^{4+} (another soft acid). This approach effectively addressed the air sensitivity issue in conventional SSEs. The strong Sn–S bonding (soft acid–soft base interaction) stabilized the (P/Sn)S_4 framework, the substituted Sn in the lattice prefers to bond with S rather than O, thereby endowing the LPSI-20Sn electrolyte with a stable crystal structure (Fig. 10a and b), enabling LPSI-*x*Sn to maintain both structural integrity and conductivity after exposure to O_2 and 10% humidity (Fig. 10c). Furthermore, the I^--rich (soft base) electrolyte layer served as an effective interfacial modification to suppress lithium dendrite growth, achieving stable cycling for over 200 hours in Li symmetric cells at 1.26 mA cm^{-2}.[146] Lu *et al.* achieved excellent air stability by substituting Sn^{4+} (soft acid) with As^{5+} (soft acid), forming stable soft acid–soft base bonds in the $[SnS_4]^{4-}$ and $[AsS_4]^{3-}$ tetrahedral structures.[147] Using CS_2 as a sulfurizing agent and low-cost oxides as raw materials, their method eliminated the need for glovebox operations (Fig. 10d and e), achieving a remarkable ionic conductivity of 2.45 mS cm^{-1} (429 times higher than the pristine material)—setting a record among all reported moist-air-stable sulfide solid electrolytes. Notably, the ionic conductivity remained recoverable (2.34 mS cm^{-1} after 280 °C heat treatment) even after exposure to humid air. Zheng *et al.* employed Bi^{3+} substitution for Sn^{4+} with its lower valence state and larger ionic radius, which increased Li^+ concentration and expanded lattice volume. This approach enhanced room-temperature ionic conductivity while reducing activation energy.[148] The stable bonding between Bi^{3+} (soft acid) and S^{2-} (soft base) effectively improved the material's air stability.

Other than doping, enhancing the air stability of sulfide electrolytes can be achieved by coating a protective layer to form a core–shell structure, preventing direct contact with air. Luo *et al.* demonstrated that a ~5 nm g-C_3N_4 coating significantly improves the air stability of Li_6PS_5Cl electrolyte by suppressing H_2S generation under humid conditions (Fig. 10f).[32] XPS analysis confirmed this protective effect: while uncoated Li_6PS_5Cl undergoes hydrolysis of PS_4^{3-} groups (evidenced by P–O bond formation), the g-C_3N_4-coated samples maintain structural integrity after air exposure (Fig. 10g). Jin *et al.* developed a core–shell structured LiF@$Li_{10}GeP_2S_{12}$ solid electrolyte *via* gas-phase fluorination (Fig. 10h and i), which maintained high ionic conductivity of 1.46×10^{-3} S cm^{-1} after 40-minute exposure to 30% relative humidity air, significantly enhancing the moisture stability of sulfide electrolytes.[21] Yu *et al.* pioneered a reversible coating strategy using 1-bromopentane amphiphilic molecules for $L_7P_2S_8Br_{0.5}I_{0.5}$ sulfide electrolyte. DFT calculations verified stronger adsorption of 1-bromopentane on the electrolyte surface (−0.85 eV) compared to H_2O (−0.62 eV), with the hydrophobic alkyl chains effectively repelling water molecules. The van der Waals-driven ultrathin (monomolecular) protective layer could be completely removed by low-temperature heating at 160 °C without compromising intrinsic electrolyte properties. This approach provided at least 40 minutes of safe processing time under humid conditions while reducing H_2S evolution by 90%, establishing a universal surface engineering strategy for moisture-sensitive sulfide materials.[149]

Both doping and coating effectively enhance the air stability of sulfide electrolytes; however, the air stability of doped sulfide electrolytes still has room for improvement. Additionally, the ionic conductivity of the coating is typically lower than that of the electrolyte, which may affect the overall ionic conductivity. Consequently, developing more robust doping protocols and optimizing coating materials with balanced protection and ionic transport properties remain critical research frontiers in sulfide-based solid-state battery development.

4.4 Stability of the interface between sulfide SSEs and electrode

Interfacial instability of sulfide-based SSEs remains a major obstacle to the realization of high-energy-density solid-state batteries. Strategies to address these interfacial issues can be pursued from either the electrode or the electrolyte side. This section focuses on electrolyte-side modifications aimed at improving interfacial stability.

Metallic lithium is considered the most promising anode material for high-energy-density lithium battery systems due to its extremely low standard electrode potential and exceptionally high theoretical specific capacity, far surpassing that of graphite. However, under the narrow electrochemical stability window of sulfide-based SSEs, lithium metal readily reduces the electrolyte into various lithium-containing compounds. For example, Li_6PS_5Cl can be reduced to Li_2S, Li_3P, LiCl, and other decomposition products. Although some of these inter-

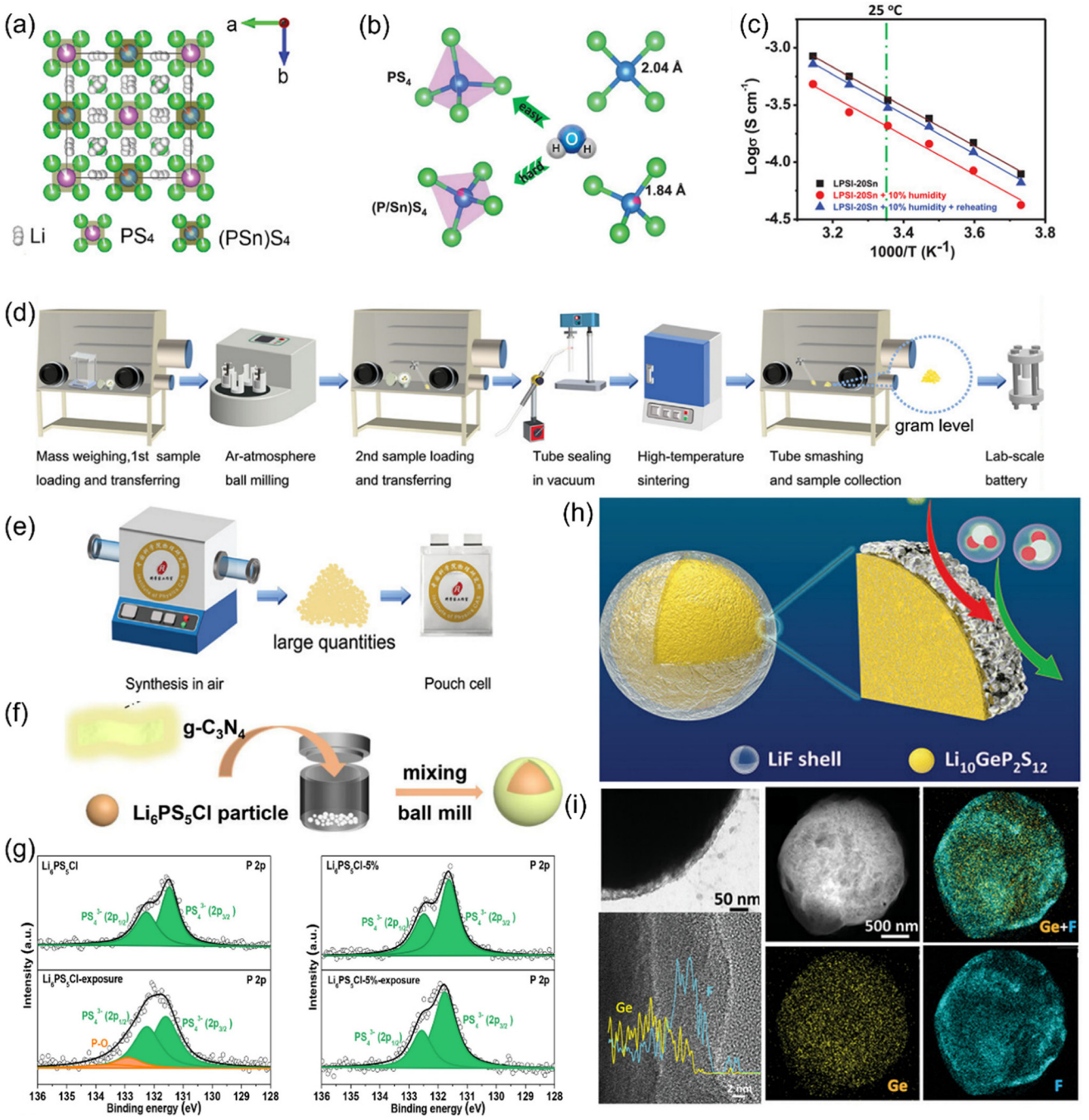

Fig. 10 (a) Structure of the prepared LPSI-20Sn.[146] (b) Schematic diagram of the degree of difficulty of being oxidized by H_2O of PS_4 and $(P/Sn)S_4$ tetrahedrons based on the DFT calculation.[146] (c) Arrhenius plots of the LPSI-20Sn electrolyte before and after exposure to air with 10% humidity, as well as after the post-heating process.[146] (d) Synthesis processes of conventional solid-phase method. This method presents several drawbacks: multistep, time-consuming, high cost, low output, and limited application.[147] (e) Synthesis processes of one-step gas-phase method in this work. This novel method presents the following advantages: one-step, time-efficient, low cost, large output, and wide application.[147] (f) Schematic diagram of g-C_3N_4 coating Li_6PS_5Cl solid electrolytes preparation.[32] (g) P 2p XPS spectra of Li_6PS_5Cl and of g-C_3N_4 coating Li_6PS_5Cl (Li_6PS_5Cl-5%).[32] (h) Schematic illustration of core–shell structured LiF@$Li_{10}GeP_2S_{12}$.[21] (i) TEM image, HRTEM and the EDS line scanning image, HAADF-STEM image and the elemental mapping images of LiF@$Li_{10}GeP_2S_{12}$.[21]

phase species may provide beneficial effects on interfacial stability, the majority contribute to increased interfacial resistance and eventual interfacial failure. Simultaneously, lithium metal anodes suffer from the notorious issue of lithium dendrite growth. Dendritic lithium formation is a major cause of short circuits and thermal runaway in conventional liquid electrolyte systems. Inorganic SSEs, owing to their high Young's modulus, are theoretically capable of suppressing dendrite

penetration. However, recent studies have demonstrated that lithium dendrites can still form and propagate even within highly dense SSEs. This is attributed to the faster Li^+ diffusion along grain boundaries, which provides favorable pathways for dendrite nucleation and growth, thereby posing a significant risk of internal short circuits.

To address these challenges, several approaches have been proposed, including the introduction of surface coatings, artificial SEI layers and protective interlayers. For instance, a composite interlayer composed of Li_6PS_5Cl (LPSC), polyethylene glycol (PEG), and LiFSI has been developed at the Li/SSE interface. This engineered interlayer leads to the *in situ* formation of a LiF-rich interphase, which effectively suppresses both electrolyte reduction and lithium dendrite growth. Additionally, the PEG component enhances the mechanical strength, ductility, and interfacial contact of the electrolyte. Symmetric cells incorporating this interface design exhibited stable cycling for over 3000 hours at 0.1 mA cm^{-2}, with a high critical current density of 4.75 mA cm^{-2}. The resulting all-solid-state LMBs (ASSLMBs) demonstrated excellent cycling stability and rate performance.[150] Yi *et al.* designed a novel sulfide-based composite solid-state electrolyte (CSE) by incorporating a LPSCl–PEO_3–LiTFSI system (97 : 3 wt/wt LPSCl : PEO), which exhibited a high ionic conductivity of 1.1 × 10^{-3} S cm^{-1} and a wide electrochemical stability window up to 4.9 V at room temperature. During the pre-cycling process, an artificial solid electrolyte interphase (SEI) layer rich in LiF and Li_3N was formed *in situ*, which effectively suppressed lithium dendrite growth and enhanced interfacial stability.[151] Gao *et al.* constructed a multifunctional SEI layer at the solid-state electrolyte interface *via* an electrochemical treatment strategy that precisely regulated the applied current and deposition time. The resulting SEI, composed of Li_3N, LiF, and Li–Si alloys, not only inhibited lithium dendrite propagation and reduced interfacial resistance but also facilitated uniform lithium nucleation and deposition. Benefiting from this engineered interphase, sym-

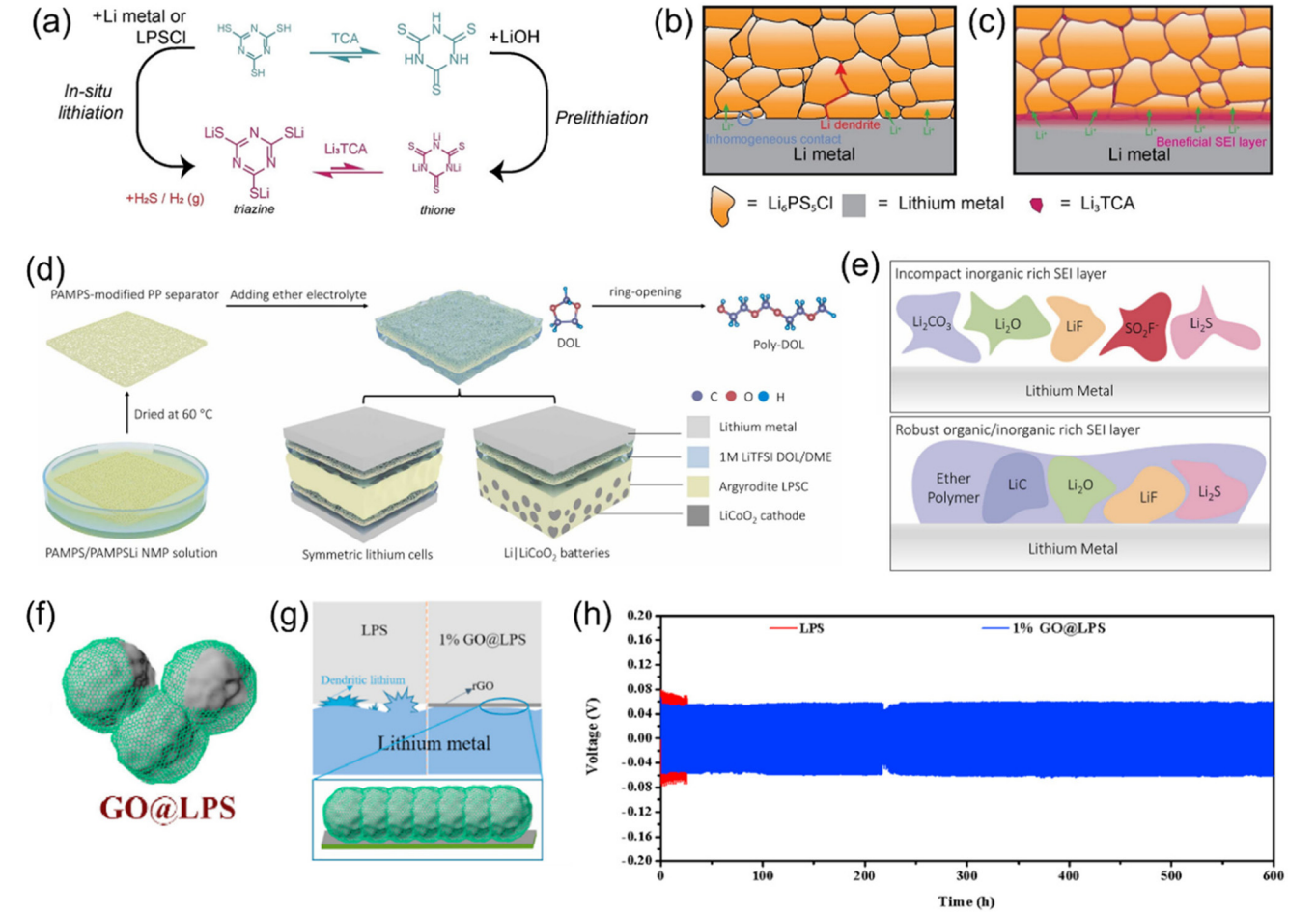

Fig. 11 (a) Trithiocyanuric acid (TCA) can be converted to lithiated trithiocyanuric (Li_3TCA) *in situ* or by prelithiation in a LiOH solution.[33] (b) The issues with sulfide-based all-solid-state batteries and (c) the presence of Li_3TCA additives creates a more P-rich, Li_2S-poor SEI layer allowing a more homogeneous Li flux.[33] (d) Schematic diagram of *in situ* polymerized interlayer of ether electrolyte for lithium anode in sulfide-based cells.[153] (e) Schematic diagrams of the SEI composition on the lithium metal.[153] (f) Schematic illustration of GO@LPS composite electrolyte.[154] (g) Schematic diagrams of GO coating to inhibit interfacial reaction between Li and bulk electrolyte.[154] (h) Li plating/stripping voltage profiles of Li/Li symmetric batteries with LPS and GO@LPS electrolyte.[154]

metric cells achieved a record-high critical current density (CCD) of 3.3 mA cm^{-2} at room temperature and exhibited stable cycling for over 1200 hours.[152]

Adding a functional additive layer between the electrode and the electrolyte to mitigate adverse interface reactions is also one of the commonly used methods to address interface issues. One strategy involves incorporating an organic additive—prelithiated trithiocyanuric acid (Li_3TCA)—into Li_6PS_5Cl to modulate interfacial chemistry (Fig. 11a). The addition of Li_3TCA alters the composition of the solid electrolyte interphase (SEI), suppressing excessive sulfide decomposition and forming a more stable and passivating interphase: a more P-rich, Li_2S-poor SEI layer allowing more homogeneous Li flux (Fig. 11b and c). This molecular-level tuning results in enhanced interfacial stability and improved cycling performance in both symmetric and full cells.[33] Another approach focuses on constructing functional interlayers. For example, an *in situ* polymerized poly-dioxolane (PDOL) interlayer has been introduced at the Li/sulfide electrolyte interface (Fig. 11d). Formed *via* ring-opening polymerization of PAMPS-loaded separators, the PDOL layer establishes good chemical compatibility with sulfide electrolytes while suppressing dendrite formation and reducing interfacial resistance. The hybrid SEI generated at this interface combines inorganic (*e.g.*, Li_2S, LiF) and polymeric components, contributing to a more robust and stable interphase (Fig. 11e).[153] These strategies—organic additive modification and polymer interlayer construction—demonstrate effective and scalable pathways for stabilizing sulfide-electrode interfaces and advancing the development of high-performance all-solid-state batteries.

Sulfide-based SSEs, while offering high ionic conductivity and favorable mechanical properties, suffer from a narrow band gap and limited electrochemical stability window. These characteristics make them susceptible to reductive or oxidative decomposition when interfaced with lithium metal or high-voltage cathodes. For instance, LGPS undergoes reduction below 1.71 V and oxidation above 2.1 V (*vs.* Li^+/Li), resulting in a narrow stability window of only ~1.71–2.1 V. Such instability can lead to irreversible structural degradation of the electrolyte and phase transformation or decomposition of the cathode. To mitigate these issues, recent studies have focused on *compositional doping* and *surface coating* strategies to enhance interfacial and electrochemical stability.

In terms of bulk doping, Peng *et al.* introduced an oxygen-substitution strategy to partially replace sulfur in $Li_{5.5}PS_{4.5}Cl_{1.5}$, synthesizing a series of O-doped electrolytes, $Li_{5.5}PS_{4.5-x}O_xCl_{1.5}$ (x = 0, 0.075, 0.175, 0.25). Among them, $Li_{5.5}PS_{4.425}O_{0.075}Cl_{1.5}$ demonstrated excellent balance between high ionic conductivity and improved interfacial compatibility under high-voltage operation. When paired with high-voltage NCM811 cathodes, the resulting ASSBs delivered stable cycling performance and high capacity retention even under elevated temperature and a cut-off voltage of 4.5 V.[155] Similarly, Liu *et al.* reported a novel borohydride-doped electrolyte, $Li_6PS_5Cl_{0.9}(BH_4)_{0.1}$, synthesized *via* mechanical ball milling and annealing. This material exhibited a significantly enhanced ionic conductivity (2.83×10^{-3} S cm^{-1}) and broadened electrochemical stability window. In contrast, F^- doping, while also improving electrochemical stability, resulted in a considerable drop in ionic conductivity (to 6.63×10^{-4} S cm^{-1}), thereby underscoring the dual benefits of BH_4^- doping in achieving both high conductivity and stability.[156]

Surface coating approaches have also shown great promise. Li *et al.* developed a graphene oxide (GO)-coated $Li_7P_3S_{11}$ SSE (GO@LPS), where the GO layer offers three-dimensional protection of electrolyte particles (Fig. 11f). The GO not only acts

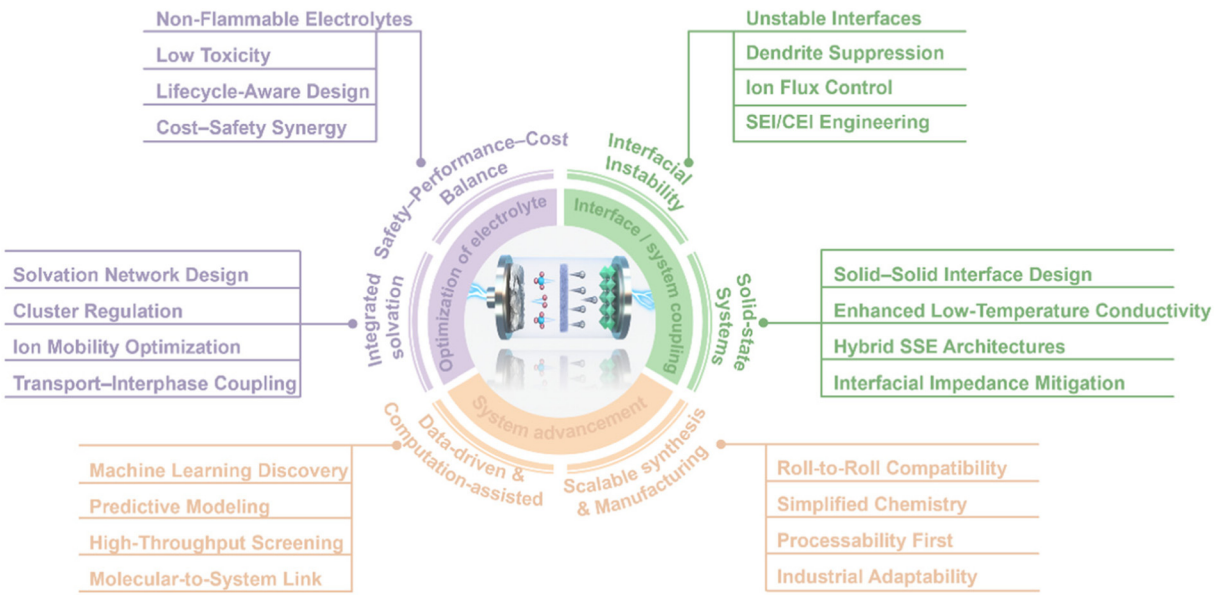

Fig. 12 Schematic illustration of future developments for high-energy-density LMBs.

as a physical barrier, mitigating direct reaction with lithium metal, but is also partially reduced to rGO during cycling, promoting homogeneous lithium deposition and enhanced interfacial stability, demonstrating superior cycling stability (Fig. 11g and h). Notably, the modified SSE remained stable under operating voltages up to 5 V, offering a new electrolyte-side protection strategy that complements conventional anode-side modifications.[154] Furthermore, atomic layer deposition (ALD) has emerged as a powerful technique for particle-level surface modification. Ultra-thin Al_2O_3 coatings deposited on Li_6PS_5Cl particles *via* ALD significantly improved moisture and air stability, reduced electronic conductivity, and enhanced interfacial contact with lithium. Electrolyte pellets fabricated from ALD-treated particles exhibited higher ionic conductivity and demonstrated stable lithium plating/stripping behavior under high current density and capacity conditions. This approach enables precise tuning of surface chemistry while preserving the bulk properties of SSEs, offering a scalable pathway for practical solid-state battery applications.[157]

Together, these advances highlight the importance of rational chemical modification and interfacial engineering in overcoming the inherent instability of sulfide-based SSEs, thereby advancing their integration into high-performance all-solid-state batteries.

5. Conclusions and perspectives

To enable ≥500 Wh kg^{-1} LMBs, electrolyte design has evolved along three main paths: liquid, polymer, and inorganic solid-state systems. Liquid electrolytes remain dominant, with advances in solvation structure and interfacial control significantly improving performance. Polymer systems offer promise due to their flexible matrices and interfacial compatibility, though room-temperature ionic conductivity still requires enhancement. Inorganic solid electrolytes feature high thermal and electrochemical stability, with ongoing efforts focused on improving interfacial contact and air stability. Across all systems, multiscale design strategies—from bulk chemistry to nanoscale interfaces—are converging to support next-generation high-energy lithium batteries.

Despite the remarkable progress achieved so far, realizing a high-energy, highly stable, and scalable electrolyte system still depends on solving the following critical issues and pursuing the corresponding directions (Fig. 12):

(1) Interfacial instability remains the dominant failure mode in practical conditions. Interfacial degradation—manifested as uncontrolled SEI/CEI evolution, dendrite formation, or ion transport inhomogeneity—limits the cyclability of LMBs under thin Li, high-voltage cathodes, and lean electrolyte configurations. Addressing this requires an interfacial design philosophy that emphasizes controlled ion flux, spatially stable interphase growth, and self-regulating architectures. Strategies should focus on precise modulation of interfacial reactions, spatial confinement of solvation structures, and construction of robust, conformal interphases compatible with both electrodes.

(2) Electrolyte design must evolve from component tuning to integrated solvation-network engineering. Rather than optimizing solvents, salts, or additives in isolation, future systems should be designed holistically to manipulate the hierarchical solvation environment—from primary coordination shells to mesoscale ionic clusters and interphase-forming precursors. This requires deeper understanding of how solvation chemistry governs ion transport, decomposition pathways, and interfacial reconstruction. The next-generation design principle is to establish stable, coordinated ion transport networks that simultaneously promote fast kinetics and interfacial passivation across full-cell architectures.

(3) Electrolyte design must achieve optimal synergy among performance, safety, and cost. While traditional research has primarily focused on energy density and cycling life, practical applications must also consider thermal runaway risks, material toxicity, environmental impact, and end-of-life recyclability. For example, the highly concentrated LiFSI/TMP system discussed in the manuscript demonstrates excellent thermal stability and SEI-forming capability, along with low volatility and non-flammability—highlighting its intrinsic safety advantages. Future electrolyte systems should incorporate inherent safety (non-flammability), low toxicity, and recyclability into their design logic, thereby advancing toward lifecycle-conscious and environmentally responsible materials systems. In particular, although fluorinated solvents and newly designed fluorinated salts such as LiFEA- or LiFPB-type chemistries offer clear advantages in interphase stabilization and electrochemical stability, their practical deployment must be judged against synthetic complexity, raw-material cost, purification requirements, and compatibility with established battery manufacturing infrastructure. Thus, future industrially relevant electrolyte development should prioritize not only performance gains, but also simplified synthesis, moderate fluorination, low additive dosage, and process compatibility with current Li-ion production lines.

(4) Data-driven and computation-assisted design will accelerate electrolyte discovery. Due to the complex coupling of chemical, electrochemical, and mechanical behaviors, empirical approaches are insufficient. The integration of machine learning, high-throughput simulation, and interfacial modeling will enable rational formulation of multi-component electrolytes with desired properties. Going forward, electrolyte design must shift toward predictive, multi-objective optimization frameworks that bridge molecular-level coordination and system-level performance.

(5) Scalable synthesis and manufacturing compatibility are critical bottlenecks. Many high-performance electrolytes rely on expensive reagents, multi-step synthesis, or processes incompatible with industrial roll-to-roll lines. These barriers must be addressed by developing chemically simplified, thermally and environmentally stable formulations and electrolyte architectures compatible with large-scale coating, stacking, and packaging methods. Processability must become a core design parameter rather than an afterthought. This is especially important for fluorinated solvents and structurally

sophisticated lithium salts, whose industrial adoption will depend not only on electrochemical merit, but also on synthetic simplicity, supply-chain accessibility, and compatibility with current large-scale battery manufacturing processes.

(6) Solid-state systems remain the most promising long-term solution, yet key barriers persist. Although solid-state electrolytes offer unmatched safety and voltage stability, they continue to face challenges in room-temperature conductivity, interfacial resistance, and mechanical/electrochemical coupling. Future work should aim to establish cohesive solid–solid interfaces, engineer mechanically compliant interlayers, and rationalize microstructure–ion transport relationships. Hybrid or gradient-structured electrolytes may serve as practical transitional architectures.

In conclusion, electrolyte design for high-energy LMBs has evolved into a multifactorial systems problem. Solving it requires the convergence of molecular engineering, interfacial physics, computational optimization, and scalable process design. Only through this integration can the next generation of LMBs achieve the performance, reliability, and manufacturability necessary for deployment across electric mobility, grid storage, and aerospace applications.

Author contributions

The manuscript was written through the contributions of all authors. All authors have given approval to the final version of the manuscript.

Conflicts of interest

The authors declare no competing financial interest.

Data availability

No primary research results, software or code have been included and no new data were generated or analyzed as part of this review.

Acknowledgements

This work is supported by the National Natural Science Foundation of China (22578392, 22408324), the Zhejiang Provincial Natural Science Foundation of China (LZ26B030003, LQ24B030002). We also thank the support from the open research fund of Suzhou Laboratory (SZLAB-1308-2024-ZD008).

References

1 C. X. Zu and H. Li, *Energy Environ. Sci.*, 2011, **4**, 2614–2624.
2 W. Zhang, Y. Song, X. Du, J. Guo, Y. Lu and X. Mao, *Chem Bio Eng.*, 2024, **1**, 678–691.
3 C. Niu, H. Lee, S. Chen, Q. Li, J. Du, W. Xu, J. G. Zhang, M. S. Whittingham, J. Xiao and J. Liu, *Nat. Energy*, 2019, **4**, 551–559.
4 Y. Zhong, Y. Su, P. Huang, Q. Jiang, Y. Lin, H. Wu, E. J. M. Hensen, A. M. Abdelkader, K. Xi, C. Lai and S. Chou, *Small Methods*, 2022, **6**, 2101613.
5 J. Jiang, M. Li, X. Liu, J. Yi, Y. Jiang, C. Wu, H. Liu, B. Zhao, W. Li, X. Sun, J. Zhang and S. Dou, *Adv. Energy Mater.*, 2024, **14**, 2400365.
6 Y. Zhong, P. Huang, W. Yan, Z. Su, C. Sun, Y. Xing and C. Lai, *Adv. Funct. Mater.*, 2022, **32**, 2110347.
7 J. Chen, H. Zhang, M. Wang, J. Liu, C. Li and P. Zhang, *J. Power Sources*, 2016, **303**, 41–48.
8 J. Guo, X. Sun, J. Xu, Y. Bian, Y. Wang, P. Jin, L. Wang and G. Liang, *Appl. Surf. Sci.*, 2023, **616**, 156534.
9 Z. Dong, J. Wei, H. Yue, K. Zhang, L. Wang, X. Li, Z. Zhang, W. Yang and S. Yang, *J. Colloid Interface Sci.*, 2021, **595**, 35–42.
10 Y. Huang, B. Wen, Z. Jiang and F. Li, *Nano Res.*, 2023, **16**, 8072–8081.
11 Q. Peng, Z. Liu, S. Chen, P. Duan, S. Cheng, L. Jiang, J. Sun and Q. Wang, *Nano Energy*, 2023, **113**, 108547.
12 S. Li, Z. Luo, L. Li, J. Hu, G. Zou, H. Hou and X. Ji, *Energy Storage Mater.*, 2020, **32**, 306–319.
13 H. Yang, J. Li, Z. Sun, R. Fang, D. W. Wang, K. He, H. M. Cheng and F. Li, *Energy Storage Mater.*, 2020, **30**, 113–129.
14 X. Wang, W. Mai, X. Guan, Q. Liu, W. Tu, W. Li, F. Kang and B. Li, *Energy Environ. Mater.*, 2021, **4**, 284–292.
15 X. Fan, L. Chen, X. Ji, T. Deng, S. Hou, J. Chen, J. Zheng, F. Wang, J. Jiang, K. Xu and C. Wang, *Chem*, 2018, **4**, 174–185.
16 S. Chen, J. Zheng, D. Mei, K. S. Han, M. H. Engelhard, W. Zhao, W. Xu, J. Liu and J. G. Zhang, *Adv. Mater.*, 2018, **30**, 1706102.
17 B. Wu, S. Wang, J. Lochala, D. Desrochers, B. Liu, W. Zhang, J. Yang and J. Xiao, *Energy Environ. Mater.*, 2018, **11**, 1803–1810.
18 M. Liu, S. Zhang, E. R. H. van Eck, C. Wang, S. Ganapathy and M. Wagemaker, *Nat. Nanotechnol.*, 2022, **17**, 959–967.
19 C. D. Quilty, D. Wu, W. Li, D. C. Bock, L. Wang, L. M. Housel, A. Abraham, K. J. Takeuchi, A. C. Marschilok and E. S. Takeuchi, *Chem. Rev.*, 2023, **123**, 1327–1363.
20 Y. N. Xu, Y. Guo, X. D. Zhang, G. F. Zhang, K. Fang, Q. F. Peng, X. Zhang, X. Z. Sun, K. Wang and Y. W. Ma, *Adv. Funct. Mater.*, 2025, **35**, 2422461.
21 Y. Jin, Q. He, G. Liu, Z. Gu, M. Wu, T. Sun, Z. Zhang, L. Huang and X. Yao, *Adv. Mater.*, 2023, **35**, 2211047.
22 R. Sudo, Y. Nakata, K. Ishiguro, M. Matsui, A. Hirano, Y. Takeda, O. Yamamoto and N. Imanishi, *Solid State Ionics*, 2014, **262**, 151–154.
23 E. J. Cheng, A. Sharafi and J. Sakamoto, *Electrochim. Acta*, 2017, **223**, 85–91.
24 W. J. Yang, A. Y. Chen, P. He and H. S. Zhou, *Nat. Commun.*, 2025, **16**, 4229.

25 Q. Chen, B. Y. Gao, Z. L. Yang, Y. Li, Q. W. Zhai, Y. Y. Jia, Q. N. Zhang, X. K. Gu, J. H. Zuo, L. Wang, T. S. Wang, P. B. Zhai, C. Yang and Y. J. Gong, *Nat. Commun.*, 2024, **15**, 10045.
26 L. Liu, Y. Li, T. Su, C. Li, Z. Hao, G. Yang and J. Ma, *Adv. Mater.*, 2025, 2508595.
27 Y. Xia, P. Zhou, X. Kong, J. Tian, W. Zhang, S. Yan, W.-h. Hou, H.-Y. Zhou, H. Dong, X. Chen, P. Wang, Z. Xu, L. Wan, B. Wang and K. Liu, *Nat. Energy*, 2023, **8**, 934–945.
28 H. An, M. Li, Q. Liu, Y. Song, J. Liu, Z. Yu, X. Liu, B. Deng and J. Wang, *Nat. Commun.*, 2024, **15**, 9150.
29 X. Jiang, Z. Liu, W. Liu, D. Yu, J. Zhang, X. Wang, Y. Zhang and S. Zhang, *Matter*, 2024, **7**, 1558–1574.
30 Z. Gao, H. Sun, L. Fu, F. Ye, Y. Zhang, W. Luo and Y. Huang, *Adv. Mater.*, 2018, **30**, 1705702.
31 S. P. Shen, G. Tang, H. J. Li, L. Zhang, J. C. Zheng, Y. Luo, J. P. Yue, Y. Z. Shi and Z. Chen, *Ceram. Int.*, 2022, **48**, 36961–36967.
32 M. Luo, C. Wang, Y. Duan, X. Zhao, J. Wang and X. Sun, *Energy Environ. Mater.*, 2024, **7**, e12753.
33 L. Braks, J. Zhang, A. Forster, P. Fritz, J. Oh, M. El Kazzi, J. W. Choi and A. Coskun, *Angew. Chem., Int. Ed.*, 2024, **63**, e202408238.
34 G. Z. Zhang, T. Zhang, Z. Zhang, R. L. He, Q. R. Wang, S. S. Chi, Y. M. Cui, M. D. Gu, Z. B. Liu, J. Chang, C. Y. Wang, K. Xu and Y. H. Deng, *Nat. Commun.*, 2025, **16**, 4722.
35 S. Huo, L. Wang, B. Su, W. Xue, Y. Wang, H. Zhang, M. Li, J. Qiu, H. Xu and X. He, *Adv. Mater.*, 2024, **36**, 2411757.
36 A. M. Li, O. Borodin, T. P. Pollard, W. Zhang, N. Zhang, S. Tan, F. Chen, C. Jayawardana, B. L. Lucht, E. Hu, X. Q. Yang and C. Wang, *Nat. Chem.*, 2024, **16**, 922–929.
37 J. Qian, W. A. Henderson, W. Xu, P. Bhattacharya, M. Engelhard, O. Borodin and J.-G. Zhang, *Nat. Commun.*, 2015, **6**, 6362.
38 G. X. Li, V. Koverga, A. Nguyen, R. Kou, M. Ncube, H. Jiang, K. Wang, M. Liao, H. Guo, J. Chen, N. Dandu, A. T. Ngo and D. Wang, *Nat. Energy*, 2024, **9**, 817–827.
39 Q. Liu, Y. Liu, Z. Chen, Q. Ma, Y. Hong, J. Wang, Y. Xu, W. Zhao, Z. Hu, X. Hong, J. Wang, X. Fan and H. B. Wu, *Adv. Funct. Mater.*, 2023, **33**, 2209725.
40 S. Chen, J. Zheng, D. Mei, K. S. Han, M. H. Engelhard, W. Zhao, W. Xu, J. Liu and J.-G. Zhang, *Adv. Mater.*, 2018, **30**, 1706102.
41 X. Ren, S. Chen, H. Lee, D. Mei, M. H. Engelhard, S. D. Burton, W. Zhao, J. Zheng, Q. Li, M. S. Ding, M. Schroeder, J. Alvarado, K. Xu, Y. S. Meng, J. Liu, J. G. Zhang and W. Xu, *Chem*, 2018, **4**, 1877–1892.
42 Y. Zhu, M. Ge, F. Ma, Q. Wang, P. Huang and C. Lai, *Adv. Funct. Mater.*, 2024, **34**, 2301964.
43 C. M. Efaw, Q. Wu, N. Gao, Y. Zhang, H. Zhu, K. Gering, M. F. Hurley, H. Xiong, E. Hu, X. Cao, W. Xu, J. G. Zhang, E. J. Dufek, J. Xiao, X. Q. Yang, J. Liu, Y. Qi and B. Li, *Nat. Mater.*, 2023, **22**, 1531–1539.
44 Z. Wen, W. Fang, F. Wang, H. Kang, S. Zhao, S. Guo and G. Chen, *Angew. Chem., Int. Ed.*, 2024, **63**, e202314876.
45 F. Chu, J. Liu, Z. Guan, R. Deng, L. Mei and F. Wu, *Adv. Mater.*, 2023, **35**, 2305470.
46 X. Wu, S. Zhang, X. Xu, F. Wen, H. Wang, H. Chen, X. Fan and N. Huang, *Angew. Chem., Int. Ed.*, 2024, **63**, e202319355.
47 Y. Zhang, Z. Yuan, B. Xie, J. Cao, H. Zhang, S. Zhang, D. Wang, F. Sun, X. Du, J. Zhang and G. Cui, *Adv. Funct. Mater.*, 2025, **39**, 2504367.
48 Z. C. Xiao, X. Liu, F. Hai, Y. Li, D. Z. Han, X. W. Gao, Z. X. Huang, Y. Liu, Z. Li, W. Tang, Y. P. Wu and S. Passerini, *Angew. Chem., Int. Ed.*, 2025, e202503693, DOI: 10.1002/anie.202503693.
49 L. Q. Wu, Z. Li, H. Li, J. Y. Zhang, Y. Li, S. X. Ren, Z. Y. Fan, X. T. Wang, K. Li, Z. Liu, J. Zhang, J. C. Yang, Y. W. Li, S. H. Bo and Q. Zhao, *J. Am. Chem. Soc.*, 2025, **147**, 16506–16521.
50 P. Li, Z. Zhang, Z. Zhao, X. Zhang, H. Zhang and G. Li, *Angew. Chem., Int. Ed.*, 2024, **63**, e202319090.
51 L. Zhang, H. Liu, T. Wang, H. Wang, D. Yan, M. Li, X. Ren, H. Li and L. Wang, *Chem. Sci.*, 2025, **16**, 13774–13783.
52 S. Zhang, R. Li, T. Deng, Q. Ma, X. Hong, H. Zhang, R. Zhang, S. Ding, Y. Wu, H. Zhu, M. Li, H. Zhang, D. Lu, B. Ma, L. Lv, Y. Li, L. Chen, Y. Shen, R. Guo and X. Fan, *Nat. Energy*, 2024, **9**, 1285–1296.
53 X. Zhang, T. Yang, Z. Huang, Q. Zhang, S. Jia, J. Kang, C. He, N. Zhao, Y. Zhang and Z. Chen, *ACS Energy Lett.*, 2025, **10**, 4428–4438.
54 J. Peng, H. Zhang, Z. Zeng, H. Zhang, H. Pei, Q. Wu, Y. Shen, R. Guo, S. Cheng and J. Xie, *Adv. Mater.*, 2025, **37**, e09109.
55 Y. Jie, S. Wang, S. Weng, Y. Liu, M. Yang, C. Tang, X. Li, Z. Zhang, Y. Zhang, Y. Chen, F. Huang, Y. Xu, W. Li, Y. Guo, Z. He, X. Ren, Y. Lu, K. Yang, S. Cao, H. Lin, R. Cao, P. Yan, T. Cheng, X. Wang, S. Jiao and D. Xu, *Nat. Energy*, 2024, **9**, 987–998.
56 H. Huang, Y. Hu, Y. Hou, X. Wang, Q. Dong, Z. Zhao, M. Ji, W. Zhang, J. Li, J. Xie, H. Guo, X. Han, X. Ouyang and W. Hu, *Nature*, 2025, **644**, 660–667.
57 L. Wu, J. Zhang, Y. Li, Z. Fan, S. Ren, J. Zhang, Y. Li, Y. Ni, W. Xie, Y. Lu, J. Chen and Q. Zhao, *Nature*, 2026, **651**, 383–389.
58 T. Tang, C. Sun, Y. Li, M. Tong, J. Lu and C. Lai, *Angew. Chem., Int. Ed.*, 2025, **64**, e202417471.
59 X. Liu, Y. Li, J. Liu, H. Wang, X. Zhuang and J. Ma, *Adv. Mater.*, 2024, **36**, 2401505.
60 Z. Hao, X. Liu, Y. Li, J. Liu, H. Li, L. Wang, G. Yang and J. Ma, *Adv. Energy Mater.*, 2025, **15**, 2502242.
61 H. Yang, Q. Liu, Y. Wang, Z. Ma, P. Tang, X. Zhang, H.-M. Cheng, Z. Sun and F. Li, *Small*, 2022, **18**, 2202349.
62 Z. Jiang, J. Liu, K. Yue, M. Pang, Y. Peng, C. Luo, Z. Yao, T. Pan, Y. Wang, Y. Li, Q. Guo, C. Zheng, W. Sun, X. Tao and S. Liu, *Energy Environ. Sci.*, 2025, **18**, 9240–9253.
63 M. Pang, Z. Jiang, C. Luo, Z. Yao, T. Fu, T. Pan, Q. Guo, Y. Li, S. Xiong, C. Zheng, W. Sun, G. Zhou and S. Liu, *Energy Environ. Sci.*, 2024, **17**, 7699–7711.

64 H. Ji, J. Xiang, Y. Li, M. Zheng, L. Yuan, Y. Liao, L. Du, Z. Li, Z. Xie, K. Huang, X. Lin, Z. Xie, Y. Shen, M. Chen, T. Li, G. Feng, Y. Sun, L. Qie, H. Li, F. Zhang, R. Guo, X. Feng, W. Chen, X. Ai, J. Lu and Y. Huang, *Nature*, 2025, **643**, 1255–1262.
65 J. Liu, B. Sun, L. Zhao, K. Liu, M. Demicoli and J. Song, *J. Am. Chem. Soc.*, 2025, **147**, 21885–21895.
66 G. Chen, L. Qiao, G. Xu, L. Li, J. Li, L. Li, X. Liu, Z. Cui, S. Zhang, S. Cheng, C. Han, S. Wang, X. Zhou and G. Cui, *Angew. Chem., Int. Ed.*, 2024, **63**, e202400797.
67 H. Sun, G. Zhu, Y. Zhu, M. C. Lin, H. Chen, Y. Y. Li, W. H. Hung, B. Zhou, X. Wang, Y. Bai, M. Gu, C. L. Huang, H. C. Tai, X. Xu, M. Angell, J. J. Shyue and H. Dai, *Adv. Mater.*, 2020, **32**, 2001741.
68 L. Qiao, U. Oteo, M. Martinez Ibañez, A. Santiago, R. Cid, E. Sanchez Diez, E. Lobato, L. Meabe, M. Armand and H. Zhang, *Nat. Mater.*, 2022, **21**, 455–462.
69 G. Mandouma, J. Collins and D. Williams, *Acc. Chem. Res.*, 2023, **56**, 1263–1270.
70 R. Miao, J. Yang, X. Feng, H. Jia, J. Wang and Y. Nuli, *J. Power Sources*, 2014, **271**, 291–297.
71 F. Qiu, X. Li, H. Deng, D. Wang, X. Mu, P. He and H. Zhou, *Adv. Energy Mater.*, 2019, **9**, 1803372.
72 X. Li, J. Zheng, M. H. Engelhard, D. Mei, Q. Li, S. Jiao, N. Liu, W. Zhao, J. G. Zhang and W. Xu, *ACS Appl. Mater. Interfaces*, 2018, **10**, 2469–2479.
73 J. Zheng, M. H. Engelhard, D. Mei, S. Jiao, B. J. Polzin, J. G. Zhang and W. Xu, *Nat. Energy*, 2017, **2**, 17012.
74 J. Alvarado, M. A. Schroeder, T. P. Pollard, X. Wang, J. Z. Lee, M. Zhang, T. Wynn, M. Ding, O. Borodin, Y. S. Meng and K. Xu, *Energy Environ. Sci.*, 2019, **12**, 780–794.
75 S. Jiao, X. Ren, R. Cao, M. H. Engelhard, Y. Liu, D. Hu, D. Mei, J. Zheng, W. Zhao, Q. Li, N. Liu, B. D. Adams, C. Ma, J. Liu, J. G. Zhang and W. Xu, *Nat. Energy*, 2018, **3**, 739–746.
76 X. Liu, C. Shen, N. Gao, Q. Hou, F. Song, X. Tian, Y. He, J. Huang, Z. Fang and K. Xie, *Electrochim. Acta*, 2018, **289**, 422–427.
77 C. Y. Son, D. Kim, S. Y. Jun, H. Park and W. H. Ryu, *Small*, 2024, **20**, 2405143.
78 S. Yan, H. Liu, Y. Lu, Q. Feng, H. Zhou, Y. Wu, W. Hou, Y. Xia, H. Zhou, P. Zhou, X. Song, Y. Ou and K. Liu, *Sci. Adv.*, 2025, **11**, eads4014.
79 H. Wang, Y. Yang, C. Gao, T. Chen, J. Song, Y. Zuo, Q. Fang, T. Yang, W. Xiao, K. Zhang, X. Wang and D. Xia, *Nat. Commun.*, 2024, **15**, 2500.
80 W. Lyu, H. Fu, A. M. Rao, Z. Lu, X. Yu, Y. Lin, J. Zhou and B. Lu, *Sci. Adv.*, 2024, **10**, eadr9602.
81 T. Hou, D. Wang, B. Jiang, Y. Liu, J. Kong, Y. He, Y. Huang and H. Xu, *Nat. Commun.*, 2025, **16**, 962.
82 J. Li, H. Hu, J. Zhu, X. Ma, Y. Hu, H. Zhang, F. Liu, S. Zhang and X. Ji, *Adv. Mater.*, 2025, **37**, 2501659.
83 J. Gou, K. Cui, S. Wang, Z. Zhang, J. Huang and H. Wang, *Nat. Commun.*, 2025, **16**, 3626.
84 Q. Zeng, J. Wang, Q. Lin, Z. Yang, M. Li, X. Zha, W. Yang and Y. Yang, *J. Mater. Chem. A*, 2025, **13**, 22849–22858.
85 H. P. K. Ngo, Y. Shao, T. Bertaux, T. K. L. Nguyen, J. Solier, E. Planes, P. Judeinstein, F. Alloin, J. Y. Sanchez and C. Iojoiu, *ACS Appl. Energy Mater.*, 2025, **8**, 2819–2827.
86 W. Lee, J. Lee, T. Yu, H. J. Kim, M. K. Kim, S. Jang, J. Kim, Y. J. Han, S. Choi, S. Choi, T. H. Kim, S. H. Park, W. Jin, G. Song, D. H. Seo, S. K. Jung and J. Kim, *Nat. Commun.*, 2024, **15**, 5860.
87 M. Newman, J. Liu, H. Jang, R. Ghosh, S. Dey, H. Cho, Y. Vodovotz, J. Sayre and M. Canova, *J. Mater. Chem. A*, 2025, **13**, 7914–7928.
88 Q. Wu, M. Fang, S. Jiao, S. Li, S. Zhang, Z. Shen, S. Mao, J. Mao, J. Zhang, Y. Tan, K. Shen, J. Lv, W. Hu, Y. He and Y. Lu, *Nat. Commun.*, 2023, **14**, 6296.
89 W. Fan, J. Gou, Y. Huang, K. She, M. Yu and Z. Zhang, *Nano Lett.*, 2024, **24**, 9050–9057.
90 D. Guo, D. B. Shinde, W. Shin, E. Abou Hamad, A. H. Emwas, Z. Lai and A. Manthiram, *Adv. Mater.*, 2022, **34**, 2201410.
91 J. K. Hu, Y. C. Gao, S. J. Yang, X. L. Wang, X. Chen, Y.-L. Liao, S. Li, J. Liu, H. Yuan and J. Q. Huang, *Adv. Funct. Mater.*, 2024, **34**, 2311633.
92 L. Yang, J. Zhang, W. Xue, J. Li, R. Chen, H. Pan, X. Yu, Y. Liu, H. Li, L. Chen and X. Huang, *Adv. Funct. Mater.*, 2022, **32**, 2200096.
93 L. Gan, X. Xu, X. Yu and H. Li, *Energy Storage Mater.*, 2025, **78**, 104223.
94 X. Y. Huang, C. Z. Zhao, W. J. Kong, N. Yao, Z. Y. Shuang, P. Xu, S. Sun, Y. Lu, W. Z. Huang, J. L. Li, L. Shen, X. Chen, J. Q. Huang, L. A. Archer and Q. Zhang, *Nature*, 2025, **646**, 343–350.
95 Y. Zhu, Z. Lao, M. Zhang, T. Hou, X. Xiao, Z. Piao, G. Lu, Z. Han, R. Gao, L. Nie, X. Wu, Y. Song, C. Ji, J. Wang and G. Zhou, *Nat. Commun.*, 2024, **15**, 3914.
96 X. Chen, C. Qin, F. Chu, F. Li, J. Liu and F. Wu, *Energy Environ. Sci.*, 2025, **18**, 910–922.
97 S. Liu, W. Tian, J. Shen, Z. Wang, H. Pan, X. Kuang, C. Yang, S. Chen, X. Han, H. Quan and S. Zhu, *Nat. Commun.*, 2025, **16**, 2474.
98 R. Gu, D. Zhang, S. Xu, X. Guo, Y. Xiao, Z. Sheng, Q. Xu, J. Xu, S. Zhu, K. Liao, S. Gong, P. Shi and Y. Min, *Nat. Commun.*, 2025, **16**, 5474.
99 W. Zhang, V. Koverga, S. Liu, J. Zhou, J. Wang, P. Bai, S. Tan, N. K. Dandu, Z. Wang, F. Chen, J. Xia, H. Wan, X. Zhang, H. Yang, B. L. Lucht, A. M. Li, X. Q. Yang, E. Hu, S. R. Raghavan, A. T. Ngo and C. Wang, *Nat. Energy*, 2024, **9**, 386–400.
100 W. Ma, X. Cui, Y. Chen, S. Wan, S. Zhao, J. Gong, G. Wang and S. Chen, *Angew. Chem., Int. Ed.*, 2025, **64**, e202415617.
101 Z. Wang, H. Wan and X. Yao, *EES Batteries*, 2025, **1**, 1122–1127.
102 Y. Wang, Z. Chen, K. Jiang, Z. Shen, S. Passerini and M. Chen, *Small*, 2024, **20**, 2402035.
103 K. Meier, T. Laino and A. Curioni, *J. Phys. Chem. C*, 2014, **118**, 6668–6679.
104 H. Xu, S. Wang, H. Wilson, F. Zhao and A. Manthiram, *Chem. Mater.*, 2017, **29**, 7206–7212.

105 J. Zhou, H. Zhu, Q. Song, Z. Ding, J. Mao, Z. Ren and G. Chen, *Nat. Commun.*, 2022, **13**, 2482.
106 N. Zhao, W. Khokhar, Z. Bi, C. Shi, X. Guo, L. Z. Fan and C. W. Nan, *Joule*, 2019, **3**, 1190–1199.
107 Y. Jin and P. McGinn, *J. Power Sources*, 2011, **196**, 8683–8687.
108 C. Deviannapoorani, L. Dhivya, S. Ramakumar and R. Murugan, *J. Power Sources*, 2013, **240**, 18–25.
109 L. Buannic, B. Orayech, J. M. López Del Amo, J. Carrasco, N. A. Katcho, F. Aguesse, W. Manalastas, W. Zhang, J. Kilner and A. Llordés, *Chem. Mater.*, 2017, **29**, 1769–1778.
110 S. Qin, X. Zhu, Y. Jiang, M. Ling, Z. Hu and J. Zhu, *Appl. Phys. Lett.*, 2018, **112**, 113901.
111 L. H. Abrha, T. T. Hagos, Y. Nikodimos, H. K. Bezabh, G. B. Berhe, T. M. Hagos, C. J. Huang, W. A. Tegegne, S. K. Jiang, H. H. Weldeyohannes, S. H. Wu, W. N. Su and B. J. Hwang, *ACS Appl. Mater. Interfaces*, 2020, **12**, 25709–25717.
112 K. Arbi, W. Bucheli, R. Jiménez and J. Sanz, *J. Eur. Ceram. Soc.*, 2015, **35**, 1477–1484.
113 C. V. Chandran, S. Pristat, E. Witt, F. Tietz and P. Heitjans, *J. Phys. Chem. C*, 2016, **120**, 8436–8442.
114 J. Liu, T. Liu, Y. Pu, M. Guan, Z. Tang, F. Ding, Z. Xu and Y. Li, *RSC Adv.*, 2017, **7**, 46545–46552.
115 D. H. Kothari and D. K. Kanchan, *Physica B: Condens. Matter*, 2016, **501**, 90–94.
116 Q. Wang, L. Liu, B. Zhao, L. Zhang, X. Xiao, H. Yan, G. Xu, L. Ma and Y. Liu, *Electrochim. Acta*, 2021, **399**, 139367.
117 Y. Inaguma, C. Liquan, M. Itoh, T. Nakamura, T. Uchida, H. Ikuta and M. Wakihara, *Solid State Commun.*, 1993, **86**, 689–693.
118 Y. Inaguma, L. Chen, M. Itoh and T. Nakamura, *Solid State Ionics*, 1994, **70**, 196–202.
119 S. Ulusoy, S. Gulen, G. Aygun, L. Ozyuzer and M. Ozdemir, *Solid State Ionics*, 2018, **324**, 226–232.
120 S. J. Lee, J. J. Bae and J. T. Son, *J. Korean Phys. Soc.*, 2019, **74**, 73–77.
121 T. Teranishi, M. Yamamoto, H. Hayashi and A. Kishimoto, *Solid State Ionics*, 2013, **243**, 18–21.
122 D. l. Lu, J. m. Ma, J. l. Wu, Y. b. Yao, T. Tao, B. Liang and S. g. Lu, *Ceram. Int.*, 2019, **45**, 2584–2590.
123 T. Teranishi, A. Kouchi, H. Hayashi and A. Kishimoto, *Solid State Ionics*, 2014, **263**, 33–38.
124 M. E. Sotomayor, A. Várez, W. Bucheli, R. Jimenez and J. Sanz, *Ceram. Int.*, 2013, **39**, 9619–9626.
125 K. Zhang, T. Xu, H. Zhao, S. Zhang, Z. Zhang, Y. Zhang, Z. Du and Z. Li, *Int. J. Energy Res.*, 2020, **44**, 9177–9184.
126 S. Chen, X. Hu, W. Bao, Z. Wang, Q. Yang, L. Nie, X. Zhang, J. Zhang, Y. Jiang, Y. Han, C. Wan, J. Xie, Y. Yu and W. Liu, *Cell Rep. Phys. Sci.*, 2021, **2**, 100569.
127 B. Davaasuren and F. Tietz, *Solid State Ionics*, 2019, **338**, 144–152.
128 X. Xu, Z. Wen, X. Yang and L. Chen, *Mater. Res. Bull.*, 2008, **43**, 2334–2341.
129 A. Rosenberger, Y. Gao and L. Stanciu, *Solid State Ionics*, 2015, **278**, 217–221.
130 L. Hallopeau, D. Bregiroux, G. Rousse, D. Portehault, P. Stevens, G. Toussaint and C. Laberty-Robert, *J. Power Sources*, 2018, **378**, 48–52.
131 Y. Luo, H. Gao and X. Zhao, *Ceram. Int.*, 2022, **48**, 8387–8394.
132 P. Odenwald, Q. Ma, B. Davaasuren, E. Dashjav, F. Tietz, M. Wolff, W. Rheinheimer, S. Uhlenbruck, O. Guillon and D. Fattakhova Rohlfing, *ChemElectroChem*, 2022, **9**, e202101366.
133 K. Kwatek, W. Ślubowska, J. Trébosc, O. Lafon and J. L. Nowiński, *J. Eur. Ceram. Soc.*, 2020, **40**, 85–93.
134 X. Zhao, Y. Luo and X. Zhao, *J. Alloys Compd.*, 2022, **927**, 167019.
135 Z. Huang, L. Chen, B. Huang, B. Xu, G. Shao, H. Wang, Y. Li and C. A. Wang, *ACS Appl. Mater. Interfaces*, 2020, **12**, 56118–56125.
136 Z. Qin, Y. Xie, X. Meng, D. Qian, D. Mao, Z. Zheng, L. Wan and Y. Huang, *ACS Appl. Mater. Interfaces*, 2022, **14**, 40959–40966.
137 Z. Qin, X. Meng, Y. Xie, D. Qian, H. Deng, D. Mao, L. Wan and Y. Huang, *Energy Storage Mater.*, 2021, **43**, 190–201.
138 A. Mei, X. L. Wang, J. L. Lan, Y. C. Feng, H. X. Geng, Y. H. Lin and C. W. Nan, *Electrochim. Acta*, 2010, **55**, 2958–2963.
139 H. Zhang, S. Hao and J. Lin, *J. Alloys Compd.*, 2017, **704**, 109–116.
140 H. Geng, A. Mei, Y. Lin and C. Nan, *Rare Met. Mater. Eng.*, 2017, **46**, 7–11.
141 K. Yu, R. Gu, L. Wu, H. Sun, R. Ma, L. Jin, Y. Xu, Z. Xu and X. Wei, *J. Alloys Compd.*, 2018, **739**, 892–896.
142 N. Kamaya, K. Homma, Y. Yamakawa, M. Hirayama, R. Kanno, M. Yonemura, T. Kamiyama, Y. Kato, S. Hama, K. Kawamoto and A. Mitsui, *Nat. Mater.*, 2011, **10**, 682–686.
143 Q. Zhang, D. Cao, Y. Ma, A. Natan, P. Aurora and H. Zhu, *Adv. Mater.*, 2019, **31**, 1901131.
144 H. Liu, Y. Liang, C. Wang, D. Li, X. Yan, C.-W. Nan and L.-Z. Fan, *Adv. Mater.*, 2023, **35**, 2206013.
145 K. H. Park, Q. Bai, D. H. Kim, D. Y. Oh, Y. Zhu, Y. Mo and Y. S. Jung, *Adv. Energy Mater.*, 2018, **8**, 1800035.
146 F. Zhao, J. Liang, C. Yu, Q. Sun, X. Li, K. Adair, C. Wang, Y. Zhao, S. Zhang, W. Li, S. Deng, R. Li, Y. Huang, H. Huang, L. Zhang, S. Zhao, S. Lu and X. Sun, *Adv. Energy Mater.*, 2020, **10**, 1903422.
147 P. Lu, L. Liu, S. Wang, J. Xu, J. Peng, W. Yan, Q. Wang, H. Li, L. Chen and F. Wu, *Adv. Mater.*, 2021, **33**, 2100921.
148 L. Zheng, J. Shi, G. Ren, T. Tang, Y. Yang, S. Shen and Z. Yao, *Energy Fuels*, 2024, **38**, 3470–3476.
149 Z. Yu, S.-L. Shang, K. Ahn, D. T. Marty, R. Feng, M. H. Engelhard, Z.-K. Liu and D. Lu, *ACS Appl. Mater. Interfaces*, 2022, **14**, 32035–32042.
150 G. G. Serbessa, B. W. Taklu, Y. Nikodimos, N. T. Temesgen, Z. B. Muche, S. K. Merso, T. I. Yeh, Y. J. Liu, W. S. Liao, C. H. Wang, S. H. Wu, W. N. Su, C. C. Yang and B. J. Hwang, *ACS Appl. Mater. Interfaces*, 2024, **16**, 10832–10844.

151 J. Yi, D. Zhou, Y. Liang, H. Liu, H. Ni and L. Z. Fan, *J. Energy Chem.*, 2021, **58**, 17–24.
152 Q. Gao, D. Wu, Z. Wang, P. Lu, X. Zhu, T. Ma, M. Yang, L. Chen, H. Li and F. Wu, *Energy Storage Mater.*, 2023, **63**, 103007.
153 G. Li, S. Wu, C. Gao, Y. Shen, H. Zheng, M. Yang, H. Liu and H. Duan, *Nano Energy*, 2024, **127**, 109786.
154 J. Li, Y. Li, J. Cheng, Q. Sun, L. Dai, X. Nie, L. Chen, G. Han and L. Ci, *Carbon*, 2021, **177**, 52–59.
155 L. Peng, S. Chen, C. Yu, C. Wei, C. Liao, Z. Wu, H.-L. Wang, S. Cheng and J. Xie, *ACS Appl. Mater. Interfaces*, 2022, **14**, 4179–4185.
156 L. Liu, H. Wang, D. Ye, H. Zhao, J. Zhang and Y. Tang, *ACS Appl. Mater. Interfaces*, 2024, **16**, 31341–31347.
157 Z. D. Hood, A. U. Mane, A. Sundar, S. Tepavcevic, P. Zapol, U. D. Eze, S. P. Adhikari, E. Lee, G. E. Sterbinsky, J. W. Elam and J. G. Connell, *Adv. Mater.*, 2023, **35**, 2300673.